

Wavelike Oscillations in High Latitude Thermospheric Doppler Temperature and Line-of-Sight Wind Observed Using All-Sky Imaging Fabry-Perot Spectrometers

R. Itani¹, M. Conde¹

¹Geophysical Institute, University of Alaska Fairbanks, Fairbanks, AK, USA

Key Points:

- Thermospheric gravity wave signatures were derived by high-pass filtering winds and temperatures acquired using optical Doppler spectroscopy
- Wave activity was almost always seen in F-region winds with a strong correlation between magnetic activity and oscillation amplitudes
- Not all oscillations were due to traveling waves, however, those that were appeared consistent with previous gravity wave observations

Corresponding author: R. Itani, ritani@alaska.edu

Abstract

Multiple years of thermospheric wind and temperature data were examined to study gravity waves in Earth's thermosphere. Winds and temperatures were measured using all-sky imaging optical Doppler spectrometers deployed at three sites in Alaska, and three in Antarctica. For all sites, oscillatory perturbations were clearly present in high-pass temporally filtered F-region line-of-sight (LOS) winds for the majority of the clear-sky nights. Oscillations were also discernible in E-region LOS wind and F-region Doppler temperature, albeit less frequently. Oscillation amplitudes correlated strongly with auroral and geomagnetic activity. Observed wave signatures also correlated strongly between geographically nearby observing sites. Amplitudes of LOS wind oscillations were usually small when viewed in the zenith and increased approximately with the sine of the zenith angle – as expected if the underlying motion is predominantly horizontal. The SDI instruments observe in many look directions simultaneously. Phase relationships between perturbations observed in different look directions were used to identify time intervals when the oscillations were likely to be due to traveling waves. However, a portion of the instances of observed oscillations had characteristics suggesting geophysical mechanisms other than traveling waves – a recognition that was only possible because of the large number of look directions sampled by these instruments. Lomb-Scargle analysis was used to derive examples of the range of temporal periods associated with the observed LOS wind oscillations. F-region wind oscillations tended to exhibit periods typically ranging from 60 minutes and above. By contrast, E-region wind oscillation periods were as short as 30 minutes.

Plain Language Summary

Atmospheric neutral wind and temperature measurements from polar regions were analyzed for two different altitudes – ~ 120 km and ~ 240 km. Ripples, also known as atmospheric gravity waves, were a nearly ubiquitous feature of winds observed in our data in the upper altitude region. Oscillations were also detected in upper region temperatures and lower region winds, although these later oscillations were weaker than those of the upper region winds. These oscillations, if visualized, would appear as a complicated wave field manifesting various sizes and propagation directions, in a manner somewhat analogous to surface waves on the ocean. Amplitudes of these oscillations responded strongly to geomagnetic activity, with large waves occurring after the onset of strong mag-

netic perturbations and persisting for several hours. Our instruments sample more than a hundred look directions in the sky at once. This allows for higher confidence in extracting wave signatures than would be possible using data from just a single look direction.

1 Introduction

Earth’s thermosphere is convectively stable and has a very high kinematic viscosity, which means that small-scale wind structures are not expected to form in the absence of strong and localized external forcing (e.g., Killeen & Roble, 1988; Killeen et al., 1988). Nevertheless, air parcels displaced vertically by local forcing would experience a restoring force due to an imbalance between buoyancy and gravity. This mechanism would allow so-called gravity waves (GWs) to propagate away from the disturbance. There is ample evidence that such waves are indeed commonly observed in the thermosphere (e.g., Hocke et al., 1996; Oliver et al., 1997; Djuth et al., 1997, 2004; Yigit & Medvedev, 2012; England et al., 2020).

Thermospheric GWs can either be generated in situ or can result from dissipation and breaking of waves propagating upward from lower atmospheric layers (Fritts & Alexander, 2003; Vadas & Fritts, 2006). In-situ generation of GWs in the auroral zone is a common outcome of geomagnetic disturbances (Oyama et al., 2001). GWs generated by mechanisms involving local energy deposition in the thermosphere typically have large relative amplitudes compared to similar waves in the lower atmosphere and have wavelengths larger than 1000 km (Garcia et al., 2016). They are thus relatively easy to observe. Observations show that large-scale thermospheric GWs occur even during quiet geomagnetic conditions suggesting that such waves may have been excited from below (Vadas & Liu, 2009; Bruinsma & Forbes, 2008). All but the largest scale of waves propagating upwards from the lower atmosphere dissipate before reaching the thermosphere. Dissipation of upward propagating waves deposits energy and momentum into the background atmosphere, which generates a broad spectrum of secondary GWs, better suited to survive in the thermosphere (Vadas & Azeem, 2020). These secondary GWs exhibit horizontal scales that are much larger than those of the primary GWs (Vadas et al., 2018).

Itani & Conde (2021) investigated an abrupt stalling of the cross-polar jet in the midnight sector over Alaska. They reported that the characteristic length scale of the stalling could be as short as ~ 200 km. Further, Innis (2000) has reported more gradual

76 stalling of the cross-polar jet. Innis (2000) suggested that one of the possible mechanisms
 77 for the stalling of the cross-polar jet could be the dissipation of gravity waves. These ob-
 78 servations suggest that gravity waves may play an important role in thermospheric dy-
 79 namics. However, details of this role are not fully understood, partly because of the dif-
 80 ficulty of observing these waves across an extended geographic region – which is one of
 81 the major motivations for the present study.

82 A number of techniques have been used for observing thermospheric gravity waves
 83 (England et al., 2020, and references therein). For example, waves cause brightness vari-
 84 ations in monochromatic (narrow-band) images of upper atmospheric airglow recorded
 85 by all-sky cameras. Low Earth orbit satellites cannot observe temporal evolution at a
 86 fixed location because of their orbital motion. Nevertheless, spacecraft can monitor wave
 87 perturbations along the orbit at what is essentially an instantaneous time because, at
 88 an average orbital speed of ~ 8 km/sec, the time taken to move a distance comparable
 89 to the wave’s horizontal wavelength is generally significantly less than the wave’s tem-
 90 poral period. However, there is no guarantee that the orbital direction is parallel to the
 91 wave’s horizontal k -vector, which means that orbiting spacecraft measure the horizon-
 92 tal trace wavelength rather than the intrinsic wavelength. Radio techniques such as ionoson-
 93 des, radars, and total electron content measured by GNSS networks can also be used to
 94 detect GWs. These methods are sensitive to wave perturbations in ionospheric electron
 95 density. Waves observed through electron density fluctuations are typically referred to
 96 as traveling ionospheric disturbances.

97 The techniques discussed above provide measurements of a number of different at-
 98 mospheric parameters. However, some of these parameters are more directly related to
 99 wave propagation than others. Temperature, wind, pressure, and mass density are the
 100 fluid fields involved in the dynamical response that allows waves to propagate. The ex-
 101 istence and characteristics of GW oscillations can be observed via perturbations in these
 102 quantities. Alternatively, other indirect proxy fields may be observed to infer the exis-
 103 tence and characteristics of thermospheric GWs. Common examples of wave detection
 104 via proxy fields would be through imaging airglow variations (Hickey et al., 2010; Fukushima
 105 et al., 2012; Paulino et al., 2016), or recording oscillatory changes in ionospheric elec-
 106 tron density (Galvan et al., 2011). The distinction between primary and proxy fields is
 107 whether the perturbations are associated with the wave’s restoring force and propaga-
 108 tion mechanism. Proxy fields play no role in the wave propagation mechanism.

2 Instruments and Methods

2.1 Instrumentation

An ordinary technique for ground-based remote sensing of thermospheric wind and temperature uses optical Doppler spectroscopy of airglow and/or auroral emissions. In this study, thermospheric winds and temperatures (and oscillatory perturbations to these quantities) were derived from Doppler shifts and Doppler broadening, measured using all-sky imaging Fabry-Perot spectrometer (FPS) instruments. FPSs have been used in several studies that have adopted this technique (e.g., Hays et al., 1969; Hernandez, 1982; Innis et al., 1996; Conde et al., 2001; Nicolls et al., 2012). However, until recently, the sensitivity of typical instruments provided limited ability to characterize the wave oscillations in the primary fields. The latest generations of FPSs now offer much-improved sensitivity. The particular implementation of the FPS technique used here is known as a Scanning Doppler Imager (SDI), which exploits high sensitivity to provide the capability to look in many directions at once. This makes wave characterization much more tractable than before. Our group has been operating SDIs for more than 20 years. In this work, SDI data have been used to extract periodic perturbations in temperature and line-of-sight (LOS) wind. Further, data were examined from instruments in both the northern hemisphere (Alaska) and the southern hemisphere (Antarctica). To our knowledge, this is the first study to compare thermospheric wave activity in both hemispheres using passive optical Doppler spectroscopy.

The object-space SDI field of view in the sky can be configured to encompass any solid angle (up to 2π steradian). The typical configuration views a zenith-centered field that extends out to about 75 degrees zenith angle. This field of view is subdivided (using image processing software) into many different contiguous sub-fields arranged in a set of concentric rings divided into sectors. The sub-fields are referred to as “zones”, of which there are 115 in total for the standard configuration. An example of the standard zone map, projected onto an altitude of 240 km, is shown in Figure 1 of Anderson et al. (2012a) for instruments located at Gakona and Poker Flat in Alaska. There are several rings (typically seven) around the zenith, and each of the rings spans 360° in azimuth. There are more azimuthal sectors in the outer rings, so the solid angles subtended by all zones are approximately similar.

Exposure times typically vary in the range of two minutes to ten minutes. Within any given exposure the SDI records the optical spectrum of the airglow/aurora for each zone, over a wavelength interval spanning approximately 10 nm, with a spectral resolution of 1 nm or less. The sky spectrum is then fitted numerically to derive the Doppler temperature and LOS component of the wind associated with each zone. An example of the resulting data acquired by an SDI observing in its standard mode is depicted in Figure 1 of Conde et al. (2018).

For the present work, SDI data were examined from three Alaskan sites (Toolik Lake, Poker Flat, and Gakona) and three Antarctic sites (Mawson, McMurdo, and the South Pole). The geographic locations of these six sites are given in Table 1. SDIs provide useful diagnostics for studying thermospheric gravity waves because they measure the temperature and wind fields that are directly associated with the wave propagation in the thermosphere (i.e. they are not proxy fields). Furthermore, the all-sky imaging capability allows the construction of 2D-geographic maps of the perturbation fields.

Table 1. Geographic locations of the six different SDI instruments deployed in Alaska and Antarctica used in this work. Coordinates have been rounded to the nearest arc minute.

Station Name	Latitude	Longitude
Toolik Lake	68° 38' N	149° 36' W
Poker Flat	65° 7' N	147° 29' W
Gakona (HAARP)	62° 24' N	145° 9' W
Mawson	67° 36' S	62° 52' E
McMurdo	77° 50' S	166° 40' E
South Pole	90° 0' S	– –

SDI instruments operate automatically and observe the sky whenever the solar depression angle exceeds 9 degrees (which is required to allow the weak airglow or auroral emissions to be isolated from the background scattered sunlight). Unfortunately, the resulting data do contain periods when the measurements are not indicative of geophysical conditions in the thermosphere – for example due to observing through the heavy tropospheric cloud or as a result of serious instrumental problems. For this study, many nights of automatically acquired data were examined. The first step in data processing

was to apply various quality parameters to select only those periods when the measurements satisfied well-established criteria for validity.

2.2 The Routine Vector Wind Product

The standard analysis of SDI spectra that satisfy the criteria for validity produces 115 estimates of the LOS component of the wind observed in each look direction. Subsequent analysis is then used to estimate zonal and meridional wind components for each zone at each time. Figure 1 shows examples of the time series of the medians of the fitted vector wind components over all 115 look directions, observed from Earth’s geographic South Pole on the night of April 10, 2018. The winds are resolved into magnetic zonal and meridional components using a Cartesian coordinate system in which the magnetic north direction is defined by the oval angle specified by the VITMO magnetic field model (<https://omniweb.gsfc.nasa.gov/vitmo/cgm.html>). Vertical bars in the top and middle panels of Figure 1 do not indicate wind uncertainties. Rather, they indicate the standard deviation of values observed in the wind components across all the zones at each time. A larger vertical bar indicates greater wind variation across the field of view.

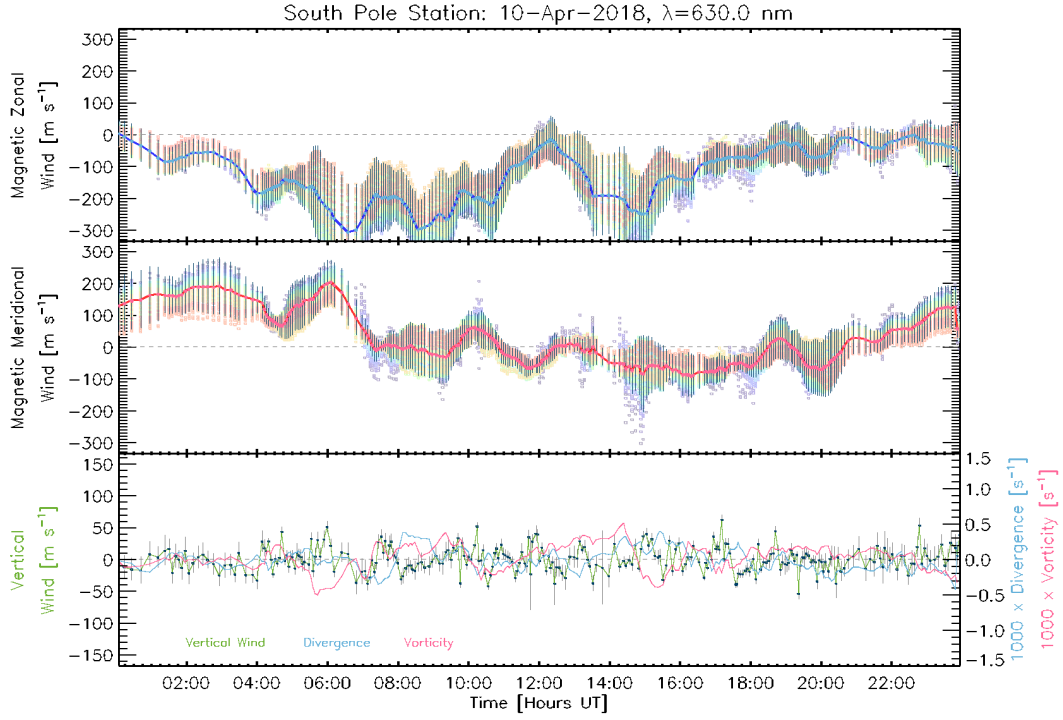


Figure 1. Wind summary plot derived from 630 nm spectra (originating from F-region heights) for the day of April 10, 2018, as observed from the Earth’s geographic South Pole. The solid blue and red traces in the top and middle panels respectively show the median of the fitted magnetic zonal and magnetic meridional winds from all look directions at a given time. Individual dots in these panels are color-coded according to the look azimuths and represent the fitted wind in each zone. The rainbow-colored swaths around the traces are composed of a number of those dots, most of which are unresolved. A few of them are discernible away from the curves. Black vertical bars on top of the median wind traces show the standard deviation of observed wind speeds in all the zones at a given time. The bottom panel shows vertical wind, horizontal divergence, and horizontal vorticity as indicated by the color of the traces. Note that geographic zonal and meridional directions are undefined at the pole. However, no such problem applies to the geomagnetic directions used here.

176 Although the fitted vector wind components are of most interest for understand-
 177 ing thermospheric dynamics at synoptic scales and larger, the fitting process generates
 178 vector components using all 115 zones together. Further, it requires several substantial
 179 assumptions (Conde & Smith, 1998; Anderson et al., 2012b). However, the horizontal
 180 wavelengths of thermospheric gravity waves are comparable to or smaller than the syn-

181 optic scale. A product derived from all look directions across the ~ 1000 km diameter
 182 field of view would suppress fluctuations that are local to one (or just a few) of the look
 183 directions. Further, the required assumptions, while reasonable when applied over the
 184 whole field of view, are almost certainly inappropriate for single-zone data. Overall, the
 185 fitted vector winds most likely would not capture wave oscillations very accurately. There-
 186 fore, for extraction of wave perturbations, it is far better to use the original LOS wind
 187 estimates, which are derived solely from the spectra observed in individual zones.

188 **2.3 Signal Processing: Extraction of Perturbations in Temperature and** 189 **LOS Wind**

190 A high-pass temporal filter was used to extract high-frequency oscillations in the
 191 observed temperatures and LOS winds. Wind and temperature perturbations were ob-
 192 tained, for each zone, as a function of time during the night. The filter transmission was
 193 tuned to begin attenuating periods longer than ~ 180 minutes. Variations over time scales
 194 longer than this are likely to reflect the slowly varying forcing experienced by the ther-
 195 mosphere as a result of changing local time, and hence may not be indicative of trav-
 196 eling waves. Additionally, oscillation periods of five minutes or less were suppressed in
 197 the current analysis to attenuate noise. Such filtering is unlikely to conceal any valid geo-
 198 physical information because 5 minutes is less than the Brunt-Väisälä period at F-region
 199 altitudes and less than or comparable to it in E-region (Yeh & Liu, 1974; Yu, 2007). Fi-
 200 nally, the sampling cadence of SDI data is typically longer than five minutes except un-
 201 der active geomagnetic conditions.

202 Figure 2 presents an example of the result of applying the high-pass filter to the
 203 115 time series of LOS winds. In this format (which is also used for a number of sub-
 204 sequent figures) high-pass filtered signals from each zone are plotted with a small ver-
 205 tical displacement between successive traces to produce a stack plot. The ordering of traces
 206 in the stack is such that the traces near the bottom correspond to zones near the zenith,
 207 whereas those near the top represent zones near the horizon. The color of the traces in
 208 the wave plots indicates the viewing azimuth relative to the magnetic north, according
 209 to the color scale bar. The sector immediately east of zero degrees magnetic azimuth is
 210 depicted with the blue hue seen at the bottom of the color scale bar. As azimuth increases,
 211 hues from progressively higher levels in the scale bar are used until the red color, which
 212 corresponds to the sector immediately west of zero degrees azimuth. Because there are

more azimuthal sectors near the horizon than near the center, the color banding is more spread near the top of the wave plots.

Many days of SDI data from various stations have been examined in this study. Wave-like oscillatory wind and temperature perturbations appeared very commonly during clear-sky observations. To illustrate the types of behavior observed, six days of data that exhibited pronounced oscillatory perturbations have been chosen from the observational archive. (As SDI instruments acquire data only during darkness, the word “day” should only be interpreted as referring to the date of observations.) Lomb-Scargle analysis was performed to find the typical periods associated with these waves.

As will be discussed in later sections, not all oscillatory perturbations seen in the data are indicative of propagating waves. The best way to unambiguously identify signatures of a propagating wave would be to reconstruct the phase fronts and the propagation directions based on phase lags between the various look directions. However, such analysis is not straightforward and is beyond the scope of this initial survey. Rather, this preliminary study will instead merely flag examples in which perturbations across a large portion of the field of view manifest phase lags that appear qualitatively consistent with a propagating wave, and determine whether such events appear to be correlated with times of elevated geomagnetic activity.

3 Results

Oscillatory perturbations were observed in LOS winds during most (if not all) of the data that passed the quality controls. In many cases, the oscillations were weak but unambiguously present. Strong oscillatory perturbations typically corresponded to times of elevated magnetic activity. These general behaviors are illustrated by the following examples.

3.1 Wavelike Perturbations in Doppler Temperatures and LOS Wind Components

3.1.1 *F-Region LOS Wind Oscillations*

The top and middle panels in Figure 2 show wavelike oscillations in LOS winds recorded by SDI instruments located at McMurdo and the South Pole stations in Antarctica, during the same night as shown in Figure 1 – i.e., April 10, 2018. These wind oscillations

were extracted from the LOS components of winds derived from 630.0 nm atomic oxygen spectra. The bottom panel shows the geomagnetic H-component recorded during this period at Scott Base, Antarctica, which is ~ 3 km from McMurdo Station. Wave activity was moderately disturbed on this day relative to the activity levels seen on many of the days in our archive. Consistent with other examples presented here, this level of wave activity was commensurate with the moderately disturbed magnetic activity on this day as indicated by the lower panel of Figure 2 and three hourly Kp indices for the observation period which were 4, 3-, 3+, 3, and 2+. The solar radio flux index (F10.7) was 68.8 solar flux unit (sfu), although there does not appear to be a strong correlation between F10.7 and wave activity within the archived observations. Note that Figure 1 shows a large-scale background wind. This has been removed from all the stack plots presented in this paper by the high-pass filtering process.

McMurdo and South Pole instruments are independent, and these stations are geographically separated by a large distance (~ 1350 km), which means that their F-region fields of view do not overlap. Nevertheless, there is some indication that the most active period in the South Pole data also corresponded to energetic wave activity at McMurdo. The amplitudes of perturbations in Figure 2 (and in subsequent LOS wind stack plots) are smallest for zones near the zenith and they increase gradually toward the outer zones closer to the horizon, as would be expected if the oscillations were primarily due to perturbations in the horizontal wind. These characteristics strongly indicate an actual geophysical origin for the wave oscillations extracted from the observations. Note that the oscillations are not simple sinusoids, illustrating that the perturbations are not monochromatic.

Importantly, the data frequently showed phase progressions among the look azimuths. Phase shifts among the oscillations arising from different parts of the sky are conspicuous in the lower panel of Figure 2 at ~ 14 UT. Another example of phase evolution in the LOS components of the wind can also be seen between 9-10 UT in the upper panel in Figure 2. In this figure, looking at the oscillations coming from similar azimuths (traces in the same color), the peak oscillations shift by ~ 15 minutes for the traces near the top of the plot relative to the traces near the bottom. This behavior is as expected considering the previously observed propagation speeds (~ 500 m/s) of storm time F-region wind oscillations (Johnson et al., 1995), and the ~ 500 km radius of all-sky field of view of the SDI instrument at 240 km altitude.

276 On this night, oscillation amplitudes recorded at McMurdo were larger than that
277 at the South Pole. Caution should be taken that the high-pass filtered wind perturba-
278 tion amplitude varies not only because of multiple look elevation angles in the field of
279 view but also due to the projection effect of various LOS wind components onto the vary-
280 ing azimuth angles of the look directions. It is quite difficult to fully resolve the contri-
281 butions of these two effects for data presented in the stack plot format.

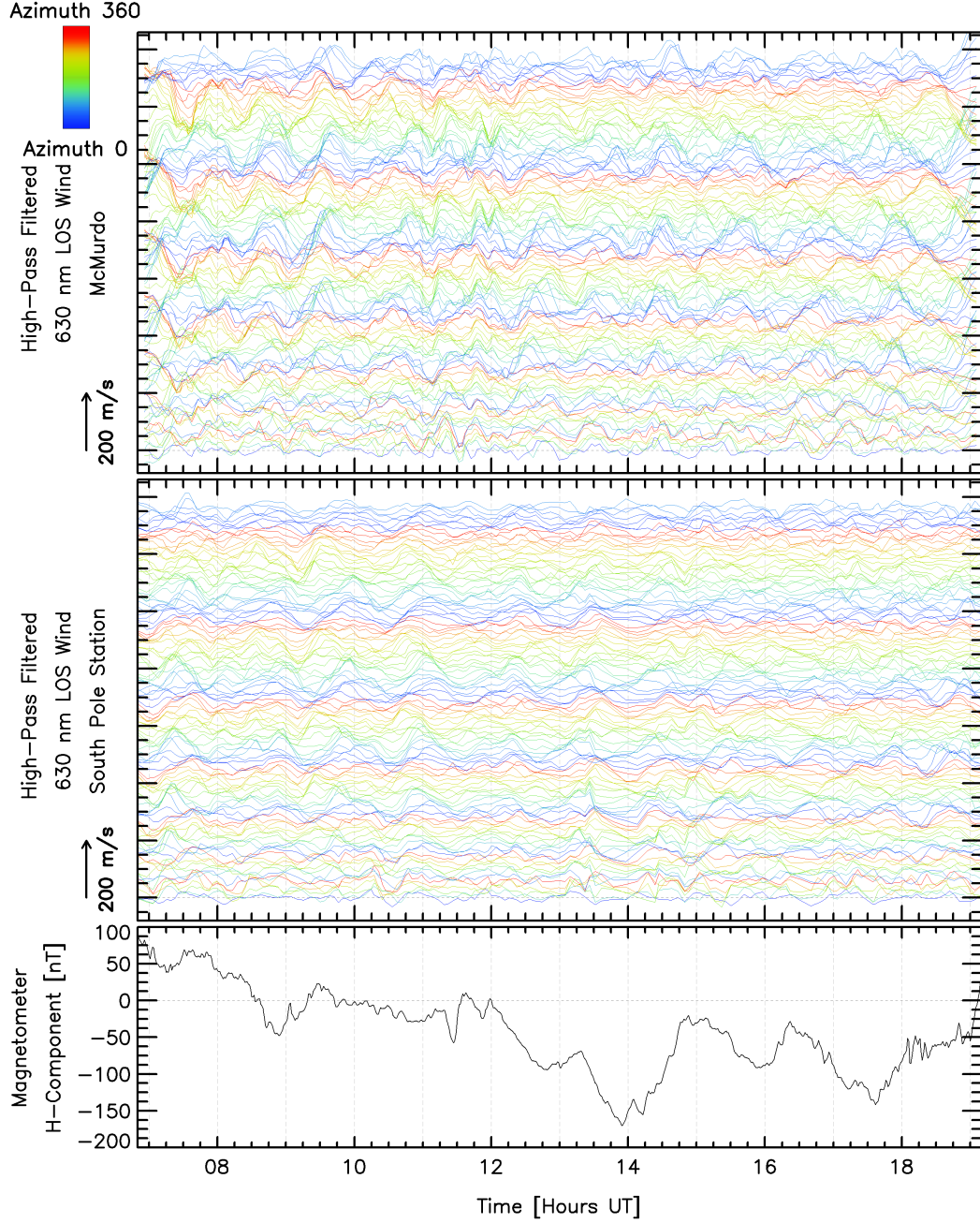


Figure 2. The top and middle panels show LOS wind oscillations observed from McMurdo and South Pole stations respectively, during the night of April 10, 2018. The magnitude of LOS wind oscillations is indicated by the scale arrow on the bottom left of each panel. The color bar on the top left shows the azimuthal directions of the zones to which the stacked wave plots correspond. Traces near the bottom of each of the top two panels correspond to zones near the zenith, whereas those toward the top represent zones near the horizon. Each field of view was divided into 115 zones, and hence there are 115 independent traces in each panel. The bottom panel shows the trace of the magnetometer H-component observed at Scott Base, Antarctica.

282 *3.1.2 Simultaneous Oscillation Signatures in LOS Wind Data Captured* 283 *by Nearby SDIs*

284 There were many instances where SDI instruments with some overlap in their field
 285 of view simultaneously observed similar oscillatory features in their high-pass filtered LOS
 286 wind data. For example, the top and middle panels in Figure 3 respectively show wave-
 287 like perturbations in F-region LOS winds as observed from Toolik Lake and Poker Flat,
 288 Alaska on October 14, 2016. The bottom panel shows the H-component of the geomag-
 289 netic field perturbation, recorded at College, Alaska, which is ~ 30 km southwest of Poker
 290 Flat. The two SDI observing sites are located ~ 400 km apart and have some overlap (more
 291 than 60 %) in their fields of view at ~ 240 km altitude. The collection and analysis of
 292 data from these two instruments are completely independent; there is no instrumental
 293 or data processing mechanism that could couple the results shown in the top two pan-
 294 els of Figure 3. Nevertheless, the time series of high-pass filtered LOS wind from each
 295 station show instances of very similar responses at times, which can only have occurred
 296 as a result of two instruments observing the same geophysical oscillations. In particu-
 297 lar, the onset of a similar burst of oscillations was observed at both sites at ~ 8 UT. Rel-
 298 atively weak wind perturbations prevailed prior to this point. However, after this time,
 299 strong wavelike oscillations persisted for the rest of the night. Note that the dynamic
 300 wave activity began within an hour of the onset of geomagnetic storm conditions. Such
 301 behavior is not unexpected. There were several occurrences in which the responses were
 302 time-synchronous across the fields of view of these two instruments. Such an instance
 303 is discernible at $\sim 8:30$ UT, at both locations, as indicated by large-amplitude responses
 304 occurring almost simultaneously across both fields of view. Such events are almost cer-
 305 tainly not indicative of propagating waves, because a field of moving wave fronts would
 306 result in responses shifted in phase between geographically separated locations. As in
 307 Figure 2, data from these sites also show a gradual increase in perturbation amplitudes
 308 from the zenith toward the horizon indicating the perturbations were associated predom-
 309 inantly with the horizontal wind.

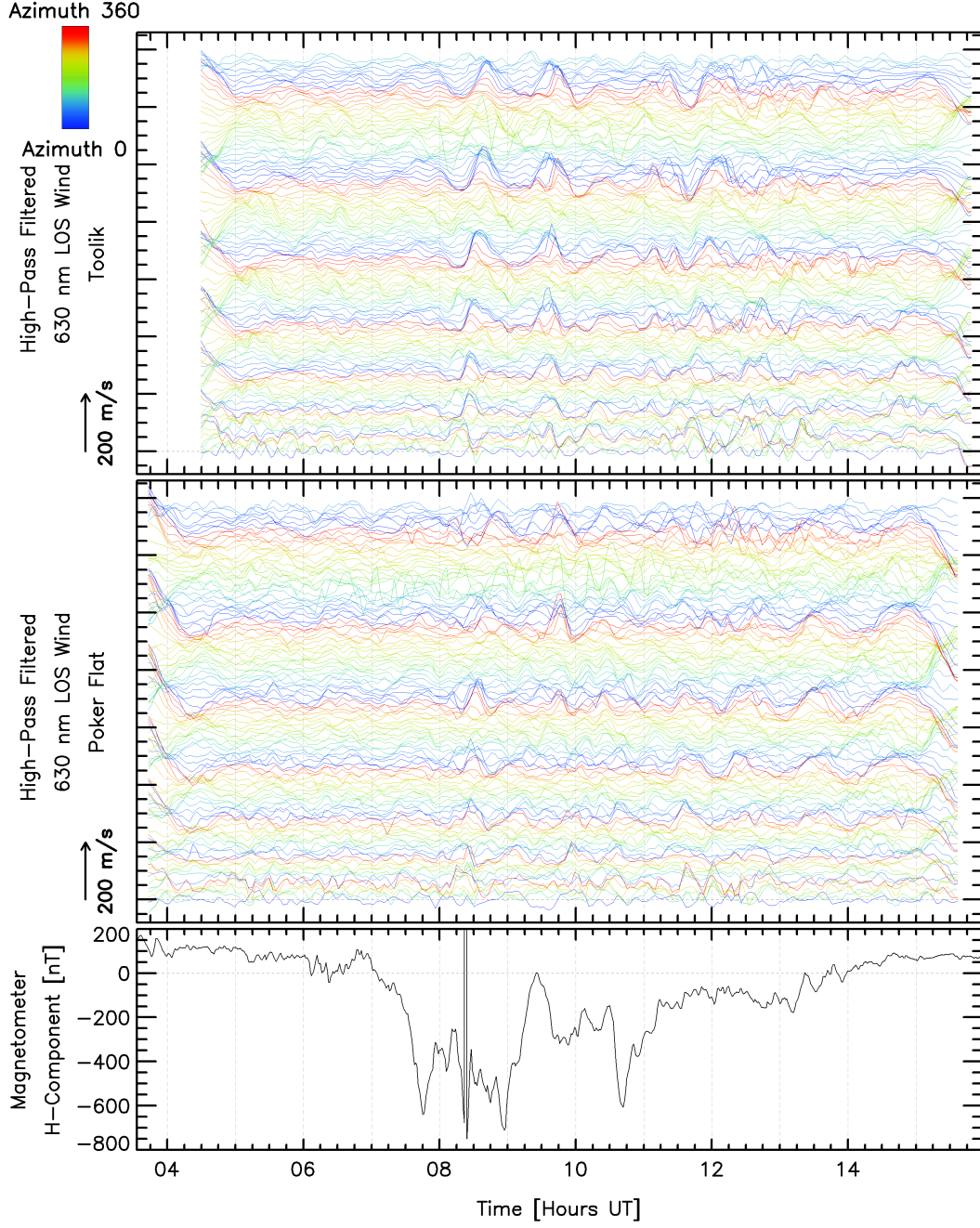


Figure 3. Same as Figure 2, but now showing measurements from Toolik Lake and Poker Flat, Alaska, for the night of October 14, 2016. The bottom panel depicts the H-component of the magnetic field perturbation recorded at College, Alaska. On this day, the F10.7 index was 92.3 sfu, and three hourly Kp indices from 3 UT to 15 UT, which also span the observation period, were 5-, 5-, 3, and 2-.

Figure 4 shows an even more dramatic example of two stations simultaneously observing remarkably similar wind perturbations. These data were recorded on January 21, 2016, again from Poker Flat and Toolik Lake. The bottom panel shows the magnetometer trace from College, Alaska, and indicates that this day was geomagnetically active. Energetic wave activity was seen in the red-line LOS wind oscillations at both locations. A qualitative examination of the time series on this night (and on other nights) suggests a strong tie between the wave oscillation amplitudes and the level of geomagnetic disturbance. As before, the two SDI instruments contributing to Figure 4 operate completely independently of each other. Wavelike perturbations that appear just before the onset of the time-synchronous event at ~ 6 UT provide an example of similar wave signatures observed from two locations. Similar responses between two nearby sites are observed commonly but not ubiquitously. Instances of similar perturbations seen from the two sites occurred throughout the night. The LOS wind perturbations were particularly highly correlated between 12 UT and 13 UT. Nevertheless, the instances of similar perturbations were superimposed on observations that were clearly independent between the two stations.

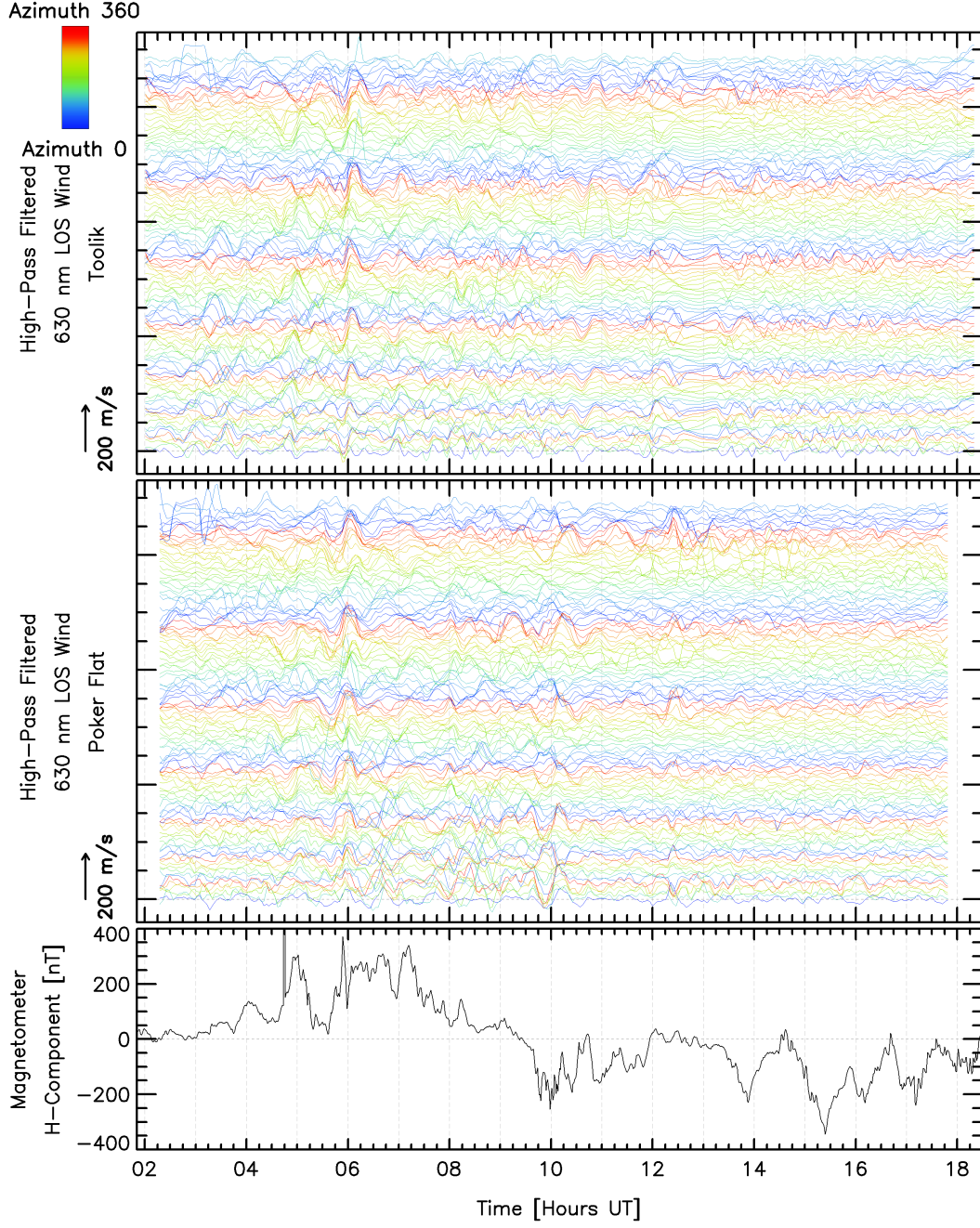


Figure 4. Same as Figure 2 but for the night of January 21, 2016, as observed from Toolik Lake and Poker Flat, Alaska. The bottom panel shows the magnetometer trace from College, Alaska. On this day, the F10.7 index was 100.7 sfu, and three hourly Kp indices for the observation period (2 UT to 18 UT) were 4-, 6-, 5+, 3+, 3-, and 4-.

3.1.3 Hemispheric Comparison of Wave Activity

For hemispheric comparison of wave activity, a two-day period was chosen for which observations were available from Mawson, Antarctica, and Toolik Lake, Alaska. Geomagnetic conditions varied considerably during this period. These two locations lie on broadly similar geographic and geomagnetic latitudes. Because of their high latitude locations, days on which both sites can observe continuously for multiple hours only occur around the equinox. Further, local time at these two sites differs by 14 hours, which means that lengthy periods of truly coincident observations do not occur because SDIs are only capable of recording sky spectra during darkness. Nevertheless, both sites made observations during the extended period shown in Figure 5. Even though the observations did not overlap in time, we can compare whether the two hemispheres responded similarly to magnetic activity.

On March 17, 2013, exceptionally high amplitude wave oscillations were observed from Toolik Lake, Alaska, and Mawson, Antarctica as a result of highly disturbed geomagnetic activity. Note that these oscillations were plotted using a less sensitive scale than other similar figures in this paper because of the large oscillation amplitudes. These were ~ 100 m/s, whereas more typical observed amplitudes were usually ~ 50 m/s or less – except, of course, during very active periods. However, on the following day, the geomagnetic disturbance declined at both sites, as did the wave activity. This result suggests that wavelike perturbation amplitudes co-vary in opposite hemispheres. However, testing for actual conjugacy would require observatories in opposite hemispheres that are located on similar longitudes to allow for observations that are truly coincident in time.

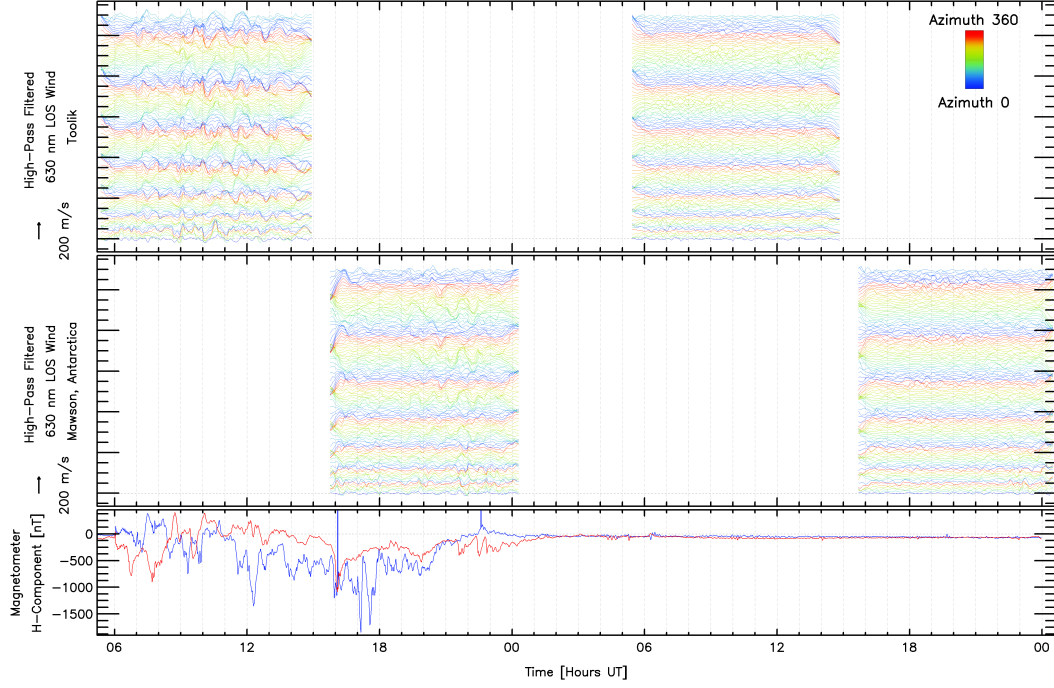


Figure 5. Same as Figure 2 but the upper two panels are showing two days of LOS wind data (March 17 to 18, 2013) from Toolik Lake, Alaska, and Mawson, Antarctica. The bottom panel shows the geomagnetic H-component recorded by the magnetometer located at College, Alaska (blue) and Mawson, Antarctica (red), as indicated by the color of the traces. The spikes in the magnetometer trace from College, Alaska near 16 UT and between 22-23 UT on March 17, 2013, are most likely due to some interference. On March 17, 2013, the F10.7 index was 124.5 sfu, and three hourly Kp indices were 2+, 7-, 6+, 6-, 6+, 7-, and 6. During the observations on March 18, 2013, the three hourly Kp indices were 3, 2+, 2, 2-, 1+, 1-, 2-, and 1+, and the F10.7 index was 116.6 sfu.

3.1.4 Wave Activity Derived from 558 nm Spectra

Figure 6 shows LOS wind oscillations derived from observations from McMurdo Station of both the thermospheric 630 nm red-line emission from the F-region, and the 558 nm green-line emission from the E-region. Strong F-region oscillations were observed throughout the night of April 10, 2018. By contrast, the E-region was mostly placid apart from a sudden packet of oscillations observed beginning at $\sim 10:00$ UT, as seen in the middle panel of Figure 6. Geomagnetic activity was disturbed throughout much of this night. The E-region wave event shown in the middle panel, however, occurred while the mag-

netometer at Scott Base observed the weakest activity over that whole night. That is, the magnetometer H -component perturbation trace was flatter and was closer to zero than at other times during the observation. Despite this, winds in the E-region manifested the largest amplitude oscillations of any time during the night.

As shown in Figure 7, the 558 nm auroral emission at ~ 10 -12 UT was associated with elevated and spatially variable Doppler temperatures. This implies that the emission was coming from generally higher in the E-region, but with considerable height variation across the field of view. Since it is known that strong vertical gradients in horizontal winds occur throughout the E-region (Larsen, 2002), the variability in observation altitude would be expected to be associated with perturbations in measured winds. This effect is likely to have contributed to the burst of oscillations seen after 10 UT. A comparison of the temperature and intensity sky maps (Figures 7 and 8 respectively) shows that the bright regions corresponded to low-energy auroral precipitation. (This is because green-line emissions in higher altitudes, corresponding to higher thermospheric temperature, are typically associated with a lower characteristic energy of electron precipitation (Hecht et al., 2006; Kaeppler et al., 2015).) Because of the elevated brightness, it seems likely that this low-energy precipitation would have carried significant energy flux (Gabrielse et al., 2021). This energy would have been deposited higher in the E-region than was the case for most other periods on this night. The heat capacity per unit volume at these higher altitudes is less (due to reduced mass density) than it would have been for the altitudes to which electron precipitation penetrated during other times of this night. The reduced heat capacity may have allowed the soft particle heating to excite pressure gradients and consequently winds, without requiring electric current, Joule heating, or any associated geomagnetic disturbance. These overall expectations are consistent with the behavior observed. A final contributor to the burst of LOS wind oscillation seen after 10 UT could be the rapidly varying auroral brightness over time, which can sometimes introduce artifacts into Doppler spectra derived from the SDI technique. This mechanism is mostly discussed here for completeness. In this particular case, it is unlikely to be the major source of the observed E-region perturbations. This is because amplitudes of the observed perturbations were the smallest for zones near the zenith, whereas the zenith zones are the ones most sensitive to spectral artifacts of this type. Care should be taken that these three effects (height variations, particle heating, and spectral artifacts) may have accounted for a significant proportion of the observed LOS wind oscil-

lations after 10 UT. The current data do not allow us to determine the relative contributions from these effects versus perturbations caused by atmospheric wave activity.

Although the magnetometer H-component was never highly disturbed, there was at least modest geomagnetic activity for the whole night. (Relevant Kp values are included in the caption for Figure 6.) Unlike the E-region, waves in the F-region occurred with large amplitudes (~ 100 m/s) for the whole night. The Scott Base magnetometer data, presented in the bottom panel in Figure 6, showed that the geomagnetic activity was more dynamic earlier in the night before SDI observations began. Presumably, the large amplitude F-region waves were triggered by this earlier activity. Alternatively, these red-line wind oscillations, with longer wave periods, dissipate slowly and thus could have propagated to the observation location from a different source region (Yigit & Medvedev, 2019). Oscillation amplitudes increased conspicuously from the zenith toward the horizon for both E-region and F-region perturbations. This zenith angle dependence indicates that the wind perturbations were primarily associated with horizontal winds.

It was initially expected that we would encounter instances of oscillations present at F-region heights as a result of waves propagating up from the lower atmosphere. In this study, the only way to identify potential wave activity driven from below would be to encounter significant wave oscillations during magnetically quiet times. Although wave activity is often present, even at quiet times, it is not possible to determine with any certainty whether small amplitude waves arose as a result of forcing from below, as opposed to being due to in-situ forcing. Of course observation of a large-amplitude wave packet during very quiet geomagnetic conditions would more strongly suggest that these waves were excited from below. However, no clear instances of large amplitude waves during geomagnetically quiet times were found in the data examined for this study. Overall, it is not possible from these data to unambiguously identify instances of forcing from below. Nevertheless, clear examples may occur after more extensive observations. Further, we may well have observed waves excited from below but have been unable to establish their origin definitively.

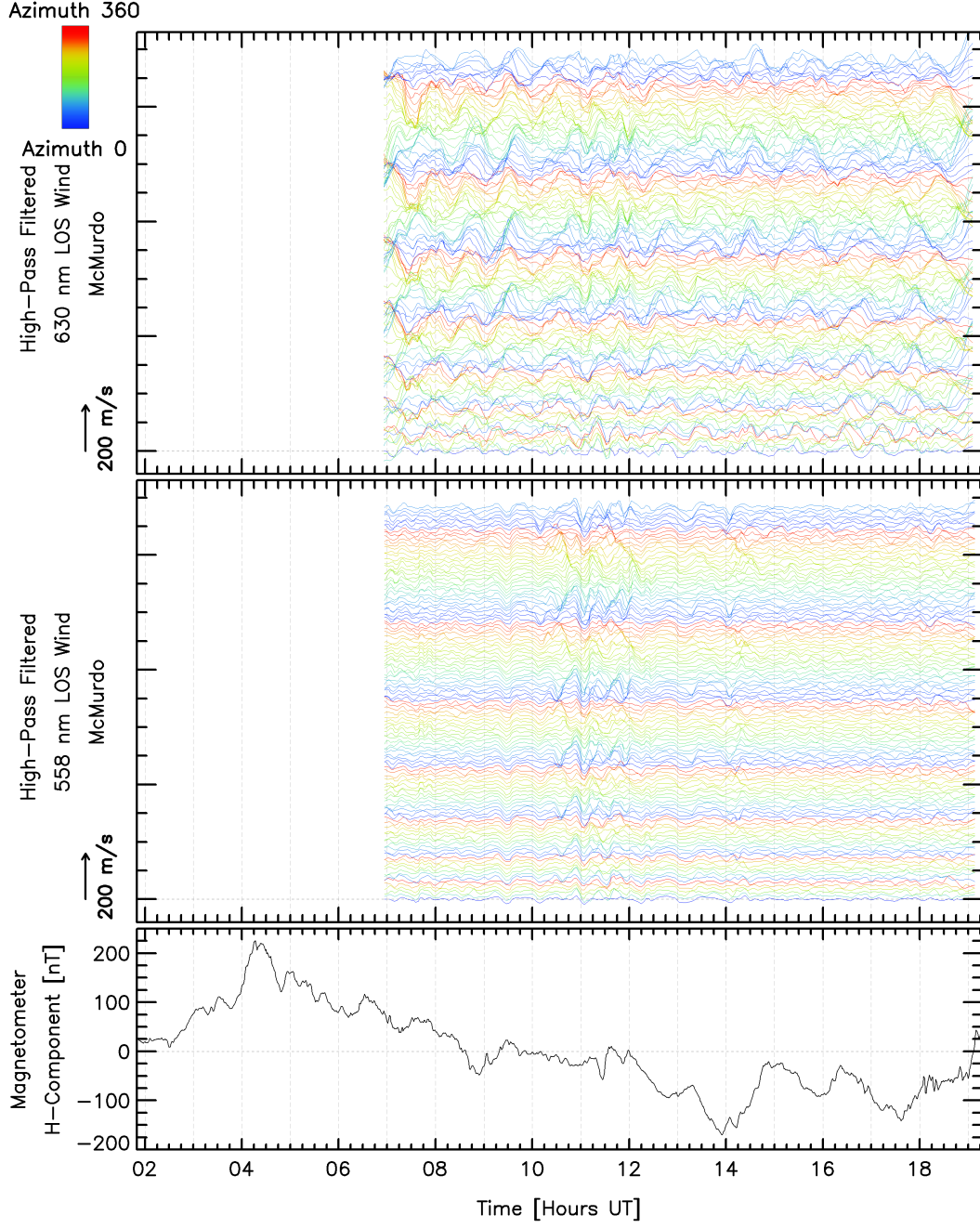


Figure 6. Same as Figure 2 but with top and middle panels respectively showing wave stack plots for F-region and E-region LOS wind perturbations observed from McMurdo Station, Antarctica on April 10, 2018. The bottom panel shows the corresponding fluctuations in the magnetic H-component recorded at Scott Base, Antarctica. On this day, the F10.7 index was 68.8 sfu, and three hourly Kp indices during the data period (6-19 UT) were 4, 3-, 3+, 3, and 2+ respectively.

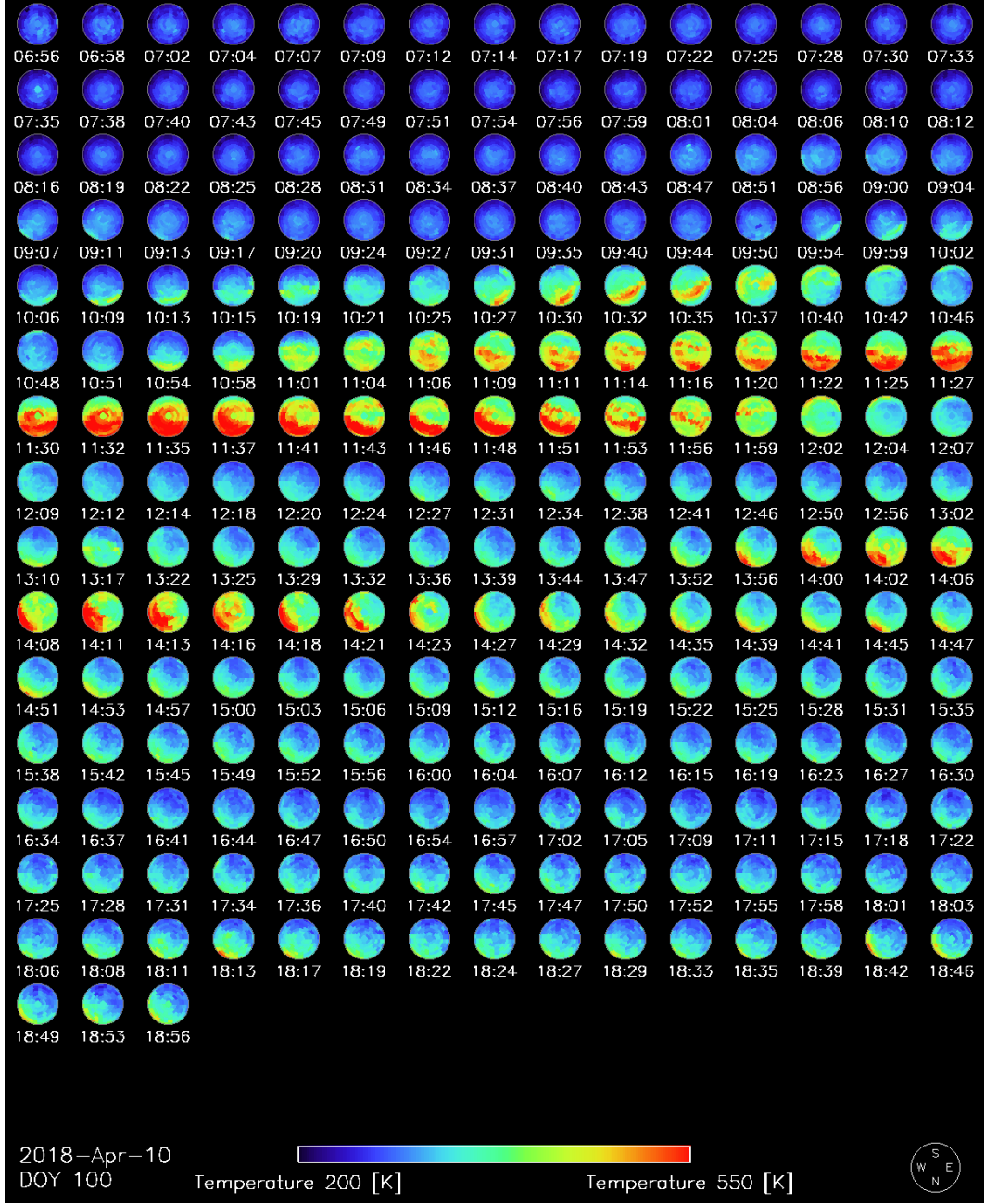


Figure 7. Skymaps of E-region Doppler temperature observed during the night of April 10, 2018, from McMurdo Station, Antarctica. Each circle shows the zenith-centered field of view of the SDI instrument at the specified time. The edge of each circle corresponds to the horizon (~ 75 degree zenith angle). Plot orientation is shown at the bottom right. The horizontal color bar at the bottom of the plot represents the temperature scale. Time in this figure is shown in the units of hours and minutes of the day in UT.

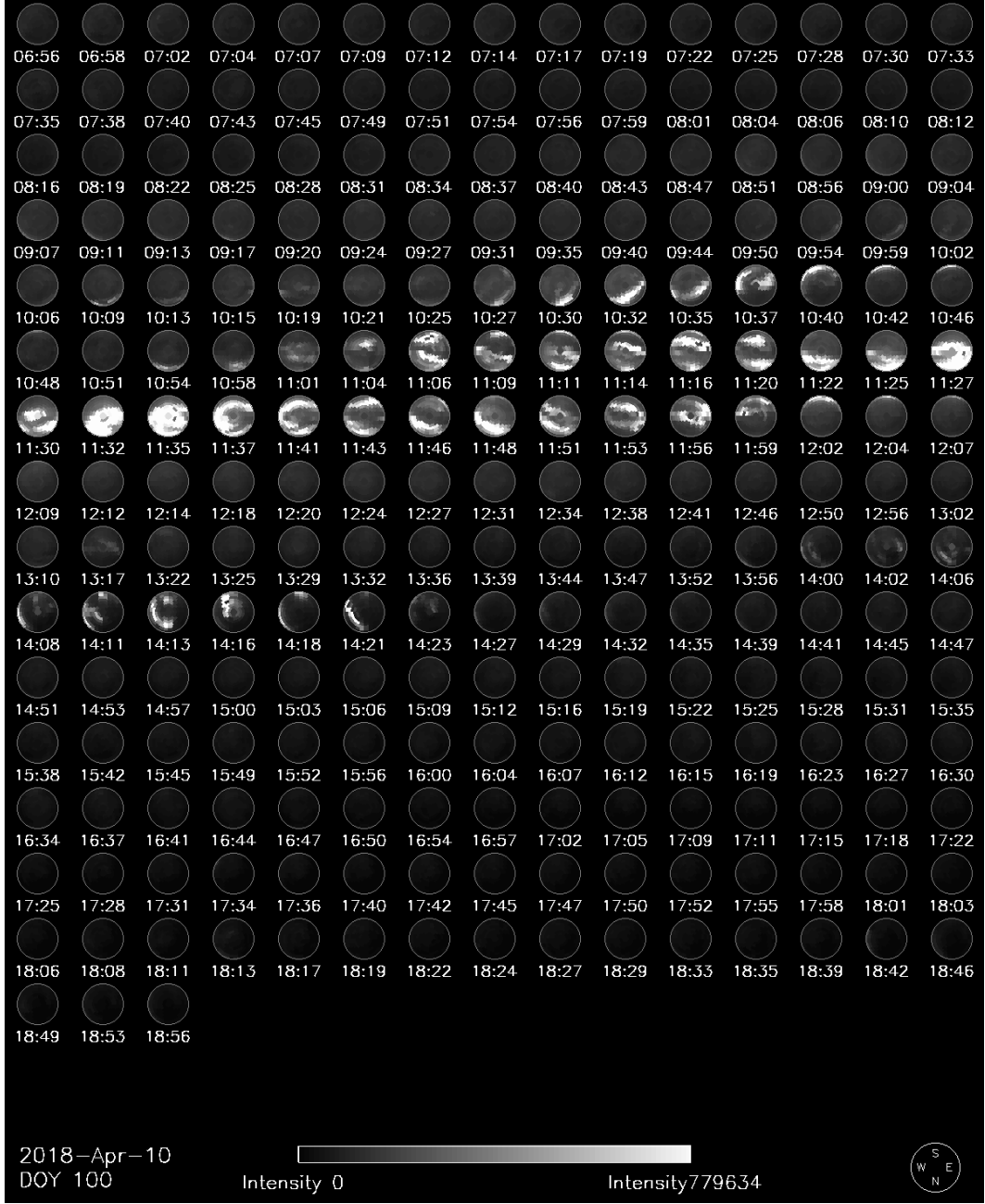


Figure 8. Same as Figure 7 but now showing skymaps of E-region airglow/auroral emission brightness displayed in arbitrary units for the night of April 10, 2018, as observed from McMurdo Station. The horizontal monochrome bar at the bottom of the plot indicates the mapping between relative brightness and gray levels.

417 **3.1.5 Concurrent Wavelike Oscillations in Temperatures and LOS Winds**

418 In addition to extracting thermospheric wind oscillations from the SDI spectra, wave-
 419 like perturbations in temperature have also been obtained. Figure 9 shows wind and tem-
 420 perature data recorded from Gakona on March 01, 2013. The wind panel shows that wave
 421 activity was relatively quiet early in the night. By contrast, large-amplitude waves pre-
 422 vailed later on this night. The middle panel shows that these wind perturbations were
 423 accompanied by temperature oscillations whose amplitude behavior over time during the
 424 night mimicked that of the winds. Qualitative inspection of Figure 9 suggests that there
 425 were several occasions with small-amplitude short-period wind fluctuations, especially
 426 between 8 UT and 9 UT. This analysis finds a typical lower cut-off period of ~ 60 min-
 427 utes for red-line LOS wind oscillations on most days. By contrast, spectral analysis of
 428 data from Gakona, Alaska on this day (not shown here for this particular day) indicated
 429 that wind oscillations occurred with statistically significant power for periods as short
 430 as ~ 30 minutes. Some of the perturbations were time-synchronous across the whole field
 431 of view; these were probably not propagating waves. On other occasions, phase progres-
 432 sions were discernible among the perturbations along different look directions. (For ex-
 433 ample phase progressions were apparent in both the wind and the temperature oscilla-
 434 tions between 14 UT and 15 UT.) It is apparent from qualitative inspection of the top
 435 panel that short-period wind oscillations were typically smaller in amplitude than long-
 436 period oscillations. Throughout the entire data set examined, magnitudes of observed
 437 oscillation amplitudes relative to experimental uncertainties were typically smaller for
 438 temperatures than they were for winds. One consequence of this is that there were fewer
 439 instances within the entire data set of unambiguous detection of wavelike activity in tem-
 440 perature, regardless of period. This difference is most extreme for shorter-period waves,
 441 for which oscillations were not typically detected in temperature, again presumably be-
 442 cause the amplitude of any short-period perturbations would not be large enough to be
 443 discernible against background noise. At times when temperature oscillations were de-
 444 tected, their amplitudes did not increase significantly from the zenith to the horizon. This
 445 is unlike the behavior observed for wind oscillations. This lack of dependence on the zenith
 446 angle for the temperature oscillation amplitudes is as expected for a scalar quantity.

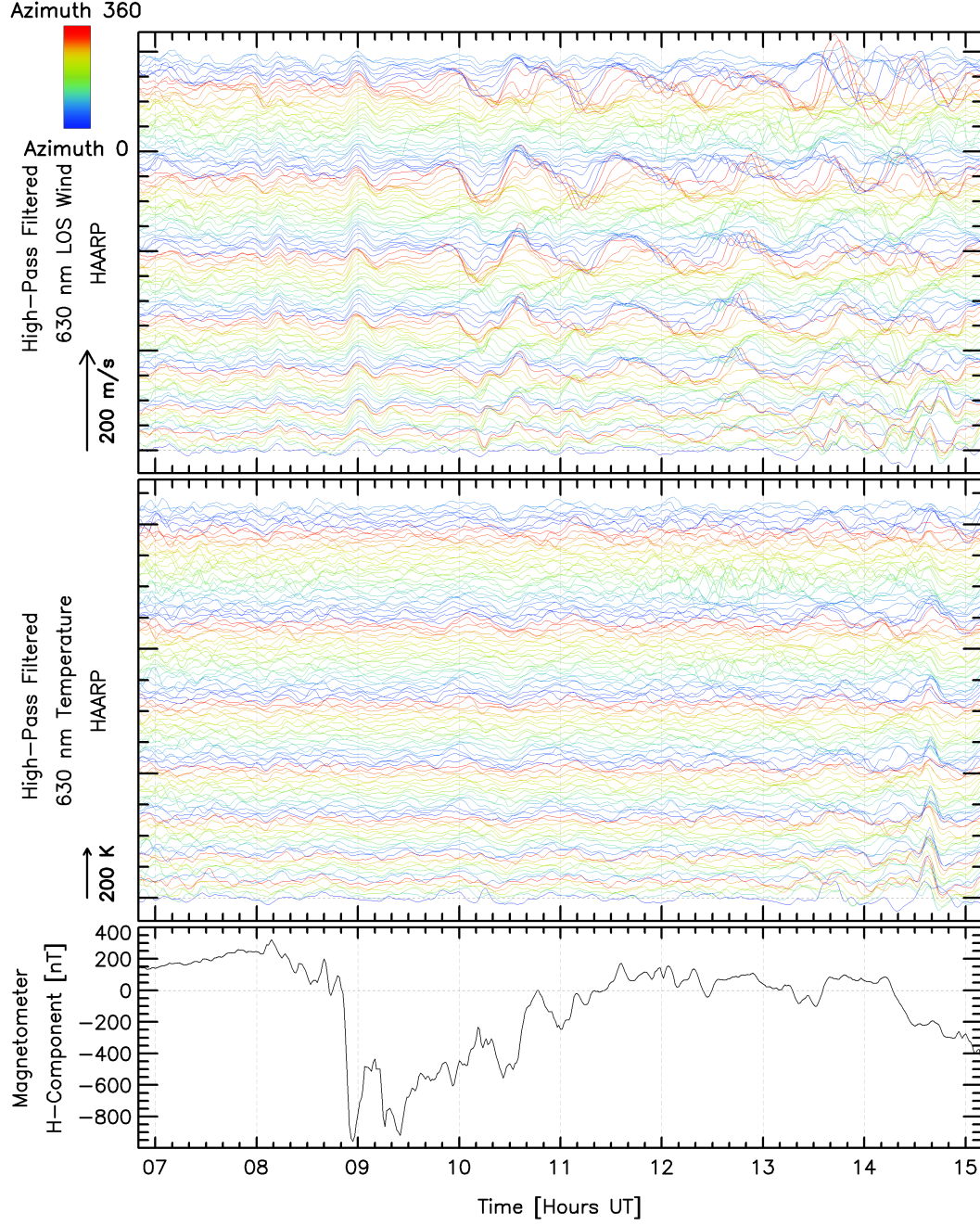


Figure 9. Same as Figure 2 but the top and middle panels respectively are showing wind and temperature oscillations recorded from Gakona, Alaska during the night of March 01, 2013. Arrows at the bottom left of the upper two panels indicate the scales of wind and temperature oscillations. The bottom panel shows the geomagnetic activity recorded at College, Alaska. On this day, the F10.7 index was 110.6 sfu, and three hourly Kp indices during (6-15) UT were 5-, 5, and 4+.

Figure 10 shows simultaneous perturbations in temperatures and LOS winds during the night of November 7, 2017, observed from Poker Flat, Alaska. Signatures of time-synchronous events, appearing as simultaneous responses occurring across almost the whole all-sky field of view, are evident on several occasions. For example, the large amplitude perturbations seen in both temperature and wind at ~ 10 UT are not signatures of propagating waves. By contrast, propagating waves would be characterized by phase progressions among the oscillations recorded along different look directions. Numerous instances of such phase progressions are noticeable in the LOS wind oscillations shown in Figure 10. An increase in the amplitude of wind oscillations toward the horizon, as seen in Figure 10 is consistent with the expectation that the perturbations were associated mostly with the horizontal wind. Note that, on this particular day, the all-sky field of view of the SDI at Poker Flat was divided into a total of 261 zones, resulting in 261 traces for wind, and similarly for temperature. (By contrast, the regular observing mode only divides the all-sky field of view into 115 zones.) There was a high correlation between the overall wave activity throughout this night with the geomagnetic activity shown in the bottom panel. Similar wave activity was observed at Toolik, Alaska as well on this night (not shown here).

By having both temperature and LOS wind perturbations, in principle, the gravity wave polarization relations could be used to infer additional characteristics of the underlying waves. However, the implementation of this analysis is not straightforward, because only the LOS component of the wind oscillations has been measured.

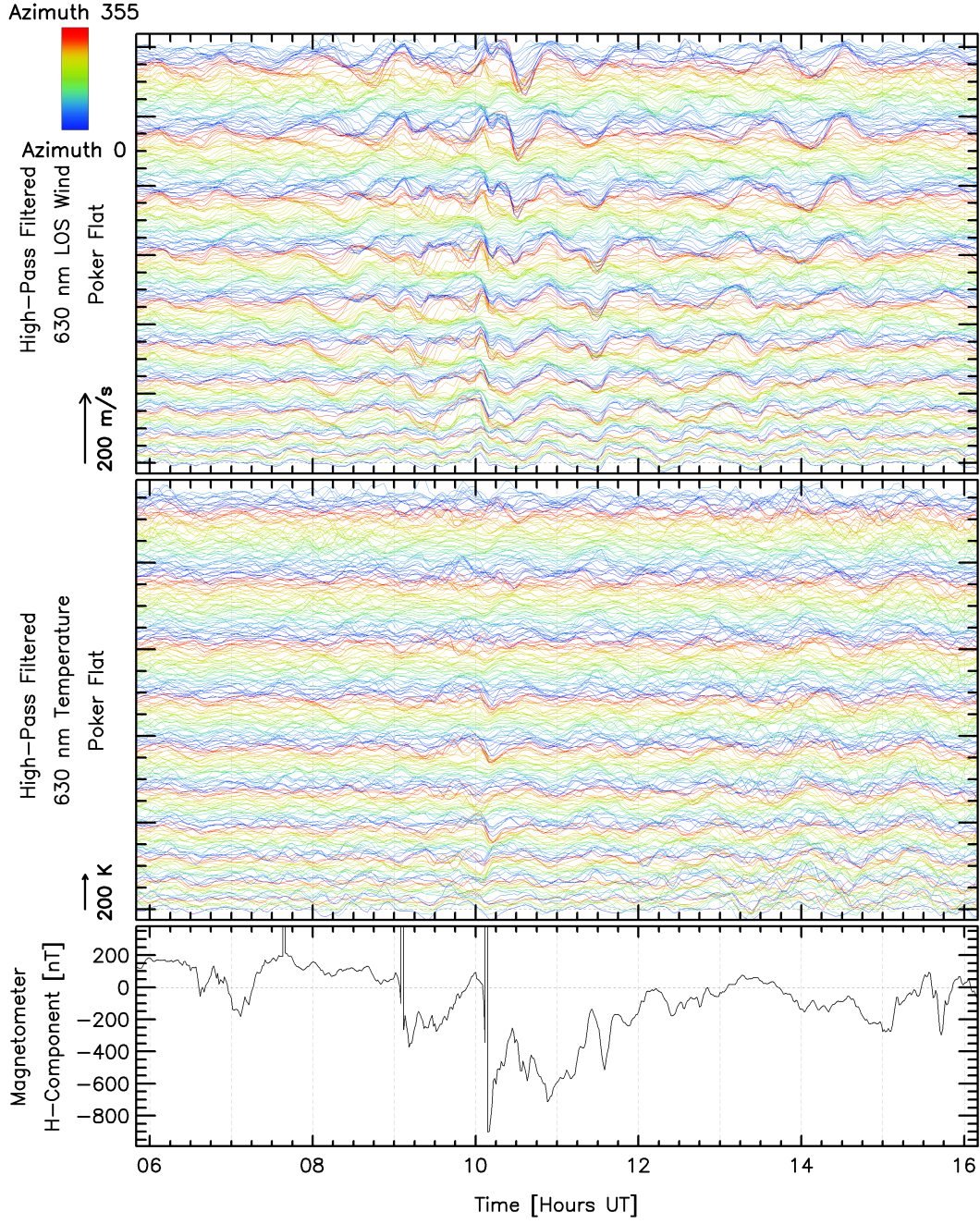


Figure 10. Same as Figure 9, but in this case showing wind and temperature oscillations as observed from Poker Flat, Alaska during the night of November 7, 2017, along with the corresponding magnetometer H-component recorded at College, Alaska. The F10.7 on this day was 67.0 sfu, and the three hourly Kp indices during (6-16) UT were 3+, 5-, 4-, and 4-.

3.2 Sliding Window Spectral Decomposition

As noted above, several previous studies have presented typical ranges of parameters for thermospheric gravity waves. In this section, estimates of temporal periods are derived from the current data to determine whether the oscillations observed here are consistent with previous observations. In the subsequent discussion, we will also consider the consistency of the horizontal wavelength, horizontal phase speeds, and relative amplitudes of the wind and temperature perturbations.

During any given night, it is to be expected that the observed wave period would vary from zone to zone and over time. Therefore, a procedure was needed that could be applied independently to a given zone and could resolve how the wave periods varied during the night. To resolve time variations, subsets of the time series for a given zone were taken using a sliding window of 180 minutes duration. The sliding window was initially centered at the time of the first measurement that occurred more than one-half of the window time after the start of observations and included all points within one-half of the window time from the center. A power spectrum of the data within the window was then calculated using the Lomb-Scargle technique (Lomb, 1976; Scargle, 1982). After each power spectrum calculation, the time series point chosen to define the window's center time was advanced by one. The final result was a set of power spectral density profiles calculated as a function of the central times of the sampling windows.

However, the resulting power spectral measurements were distributed non-uniformly in time. SDI instruments self-adjust their exposure time depending on the brightness of the optical airglow/auroral emission. Since the brightness changes over time, the corresponding temperature and LOS wind observations are not uniformly spaced in time, which is why the Lomb-Scargle approach was used rather than the more common fast Fourier transform method.

Example results are shown for a selected day. To render these data as a false-color 2-D image, the power spectra were thus interpolated onto a regular time grid. Overall, this allowed us to plot, for any selected zone, the power spectral density as a function of wave period and universal time during the night. This result is referred to as a “dynamic spectrum.”

Note that the all-sky field of view is typically divided into 115 different zones. For a given night, a separate dynamic spectrum can be produced for each of those zones, or, alternatively, an all-sky dynamic spectrum can be generated by averaging the power spectra from each zone. In the discussion below, one example is presented of the dynamic spectrum computed from a single zone over one night, for both red-line and green-line observations. The corresponding all-sky averaged dynamic spectra for both (red-line and green-line) observations on the same night are also presented. It is important to realize that the all-sky plots were produced by averaging the power spectra, rather than computing a single power spectrum from the LOS wind time series averaged over all zones. Because the wind component used here is aligned with the instrumental line-of-sight, averaging this component over the whole sky would be undesirable, as this would typically suppress most of the geophysical information present in the original measurements.

3.2.1 Spectral Decomposition of E-region LOS Wind Oscillations

Figures 11 and 12 show examples of dynamic spectra for the night of April 10, 2018, corresponding to E-region winds as observed from McMurdo Station, Antarctica. In these figures, x-axes represent universal time in hours while the y-axes represent wave periods in minutes. The fill colors are related to the power spectral density in arbitrary units, as indicated by the color bar on the right. The black horizontal indicator line in the color bar represents the level above which the estimated power spectral density is greater than the noise, to a statistical confidence of 95%.

Figure 11 represents a single zone (zone number 100), centered approximately at geographic longitude: 165.53° and geographic latitude: -75.72° . This particular zone was chosen because the range of periods containing significant power varied considerably during the observations in this zone. Several spectral features appeared in this zone during the observations on this day. By contrast, there were other zones where the band of significant power remained relatively constant over time. The location of the selected zone within the all-sky field of view is shown at the bottom right by red highlighting in a small zone map. In this zone, wave periods during the observation ranged from ~ 30 minutes to as long as more than ~ 220 minutes. Oscillations with periods centered around 85 minutes prevailed for more than 5 hours during the night. The duration of 5 hours is more than three times the 85 minutes wave period.

Figure 12 shows the dynamic spectrum averaged over all the 115 zones for E-region winds observed on the same night and from the same location as in Figure 11. This all-sky dynamic spectrum is rather simply structured, with just one significant wind oscillation, corresponding to periods ranging from ~ 100 minutes to ~ 220 minutes. Shorter-period oscillations, such as those observed in zone 100 (Figure 11), did not appear in the all-sky dynamic spectrum. These short-period oscillations were examined across all the zones during the night and it was found that those oscillations were present only in about twenty zones that were away from the zenith in the western portion of the field of view. Further, shorter-period oscillations were observed to have smaller amplitudes than longer-period oscillations. Subsequently, such weaker oscillations were washed out as a result of averaging the dynamic spectra across all the zones. The fact that a cluster of waves with a band of periods prevailed only in a small number of zones (i.e., ~ 20) strongly suggests that the corresponding oscillations were not instrumental artifacts. The optical configuration of the SDI instruments is such that signal originating from every viewing zone illuminates the entire aperture of the etalon. This means that any artifacts resulting from unstable etalon behavior would affect all zones. There is no mechanism by which etalon instability could only impact a small subset of zones. This means that oscillations seen in a small subset of zones are unlikely to be of instrumental origin.

On this night, the majority of the power was centered among oscillations with periods in the range spanning ~ 120 - 160 minutes. The long-period cutoff appeared less sharp relative to that for the shorter-period oscillations. However, this is most likely a consequence of the longest periods shown in Figure 11 becoming comparable to the width of the sliding time window, which has the effect of reducing the spectral resolution achievable for the longest periods shown. Longer-period oscillations, centered around 150 minutes, detected in zone 100 were visible in the all-sky dynamic spectrum shown in Figure 12 as well.

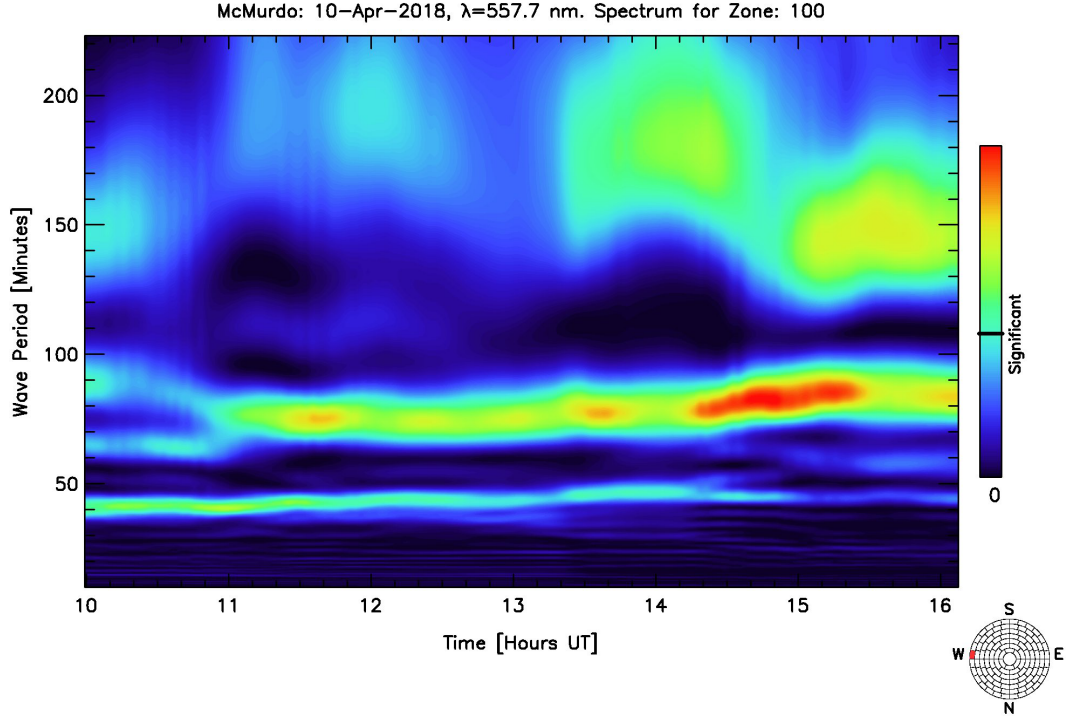


Figure 11. Dynamic Spectrum corresponding to zone number 100 for E-region winds during the night of April 10, 2018, as observed from McMurdo Station, Antarctica. Power spectral density (in arbitrary units) is represented using blue through red hues, as indicated by the color scale bar at the right. The horizontal black line on the color bar indicates the level above which there is less than 5 % probability that power calculated by the Lomb-Scargle analysis was derived solely from random noise. The small zone map at the bottom right indicates (in red highlighting) the zone chosen for the spectral decomposition.

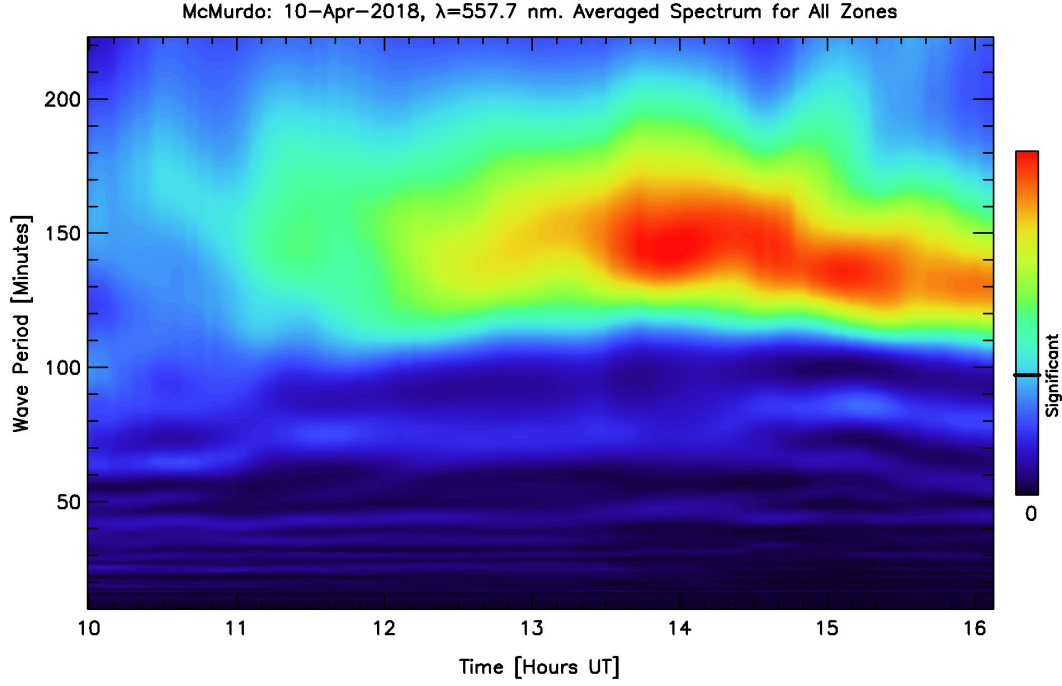


Figure 12. Green-line periodogram for the same day as Figure 11, but averaged over the whole field of view. In this case, the power spectral densities were calculated for each zone during the night and then averaged.

555 3.2.2 Spectral Decomposition of F-region LOS Wind Oscillations

556 Figures 13 and 14 show dynamic spectra for F-region winds as observed from Mc-
 557 Murdo Station, Antarctica during the same night (i.e., April 10, 2018) as the green-line
 558 winds presented earlier. Figure 13 represents the dynamic spectrum derived from just
 559 one zone, zone number 52, centered approximately at geographic longitude: 165.04° and
 560 geographic latitude: -75.57° . This zone at F-region altitude corresponds to a similar ge-
 561 ographic location as zone 100 for E-region observation shown earlier. For this zone, wave
 562 periods carrying significant power ranged over the whole night from ~ 60 minutes to more
 563 than 220 minutes. However, most of the time, the wave periods of the statistically mean-
 564 ingful oscillations were more confined, spanning only the approximate range from 90 to
 565 210 minutes. Although wave amplitudes at periods shorter than those mentioned above
 566 for each altitude region were detected at times, such occasional occurrences are likely due
 567 to the high-end tail of the noise distribution, given that the indicated confidence level
 568 is rarely substantially greater than the chosen threshold of 95 %. The most significant
 569 power was observed shortly after 12 UT for periods centered around 90 minutes and af-

570 ter ~ 13 UT for periods centered around 180 minutes. As was the case of the E-region
 571 wind oscillations shown previously, the Lomb-Scargle analysis yielded lower spectral res-
 572 olution for longer periods (again as expected). Oscillations with periods less than ~ 60
 573 minutes at F-region altitudes were rarely detected in the SDI data. This is understood
 574 to be the consequence of the mechanisms for the generation and dissipation of waves in
 575 the F-region. These estimates lie within the range previously reported (e.g., Miyoshi et
 576 al., 2018). However, spectral analysis of the time series of LOS winds derived from 558
 577 nm emission (which originates at lower E-region heights) did commonly identify shorter-
 578 period (as short as ~ 30 minutes) oscillations (e.g., Figure 11).

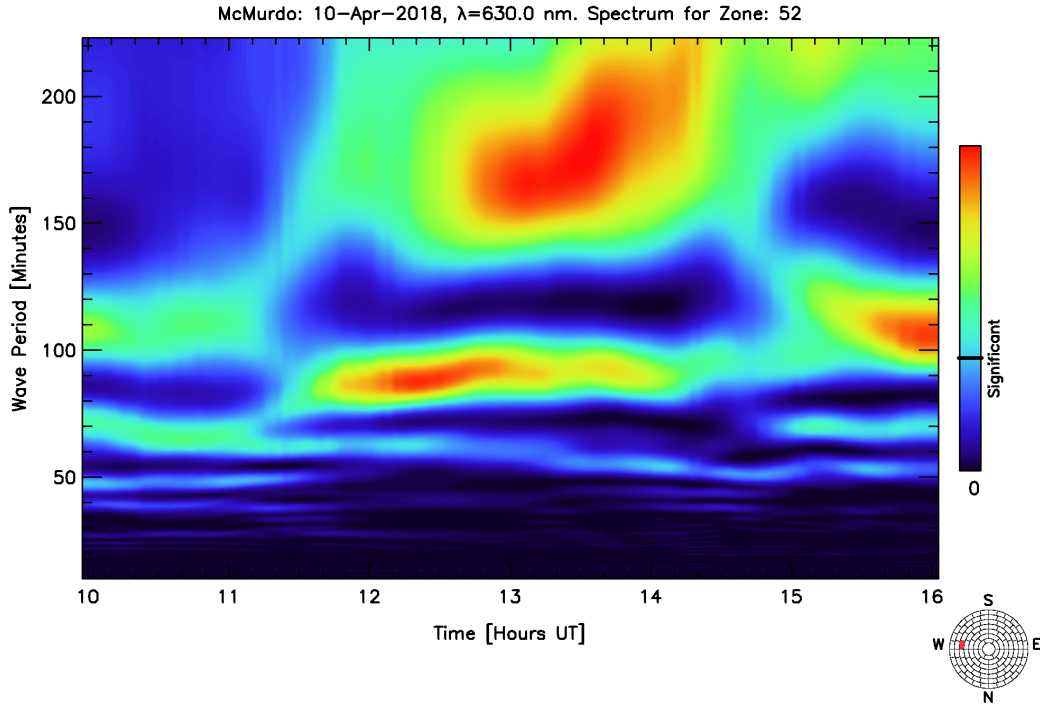


Figure 13. Same as Figure 11 but corresponding to F-region winds as observed from McMurdo Station, Antarctica on April 10, 2018, in zone number 52. The zone map at the bottom right shows, in red highlighting, the zone chosen for this dynamic spectrum plot.

579 Figure 14 shows the dynamic spectrum for F-region winds averaged over the whole
 580 field of view of the SDI instrument located at the McMurdo Station during the night of
 581 April 10, 2018. As in the previous case of E-region winds, some of the weak oscillations
 582 seen in a single zone were washed out as a result of averaging the dynamic spectra over

583 the whole sky. The band of red and green colors apparent in this plot reflects the large-
 584 scale picture of the wave activity during the night. The lowest significant period detected
 585 in the all-sky F-region LOS wind periodogram on this day was ~ 60 minutes. As before,
 586 the long-period boundary of the band of statistically significant power for F-region wind
 587 oscillations was not as sharp as the short-period boundary, again presumably as a con-
 588 sequence of limited spectral resolution for long periods. Periods where the power spec-
 589 tral density was prominent in zone 52 (Figure 13) were largely conspicuous in the all-
 590 sky dynamic spectrum as well, indicating that these oscillations were present in most zones.

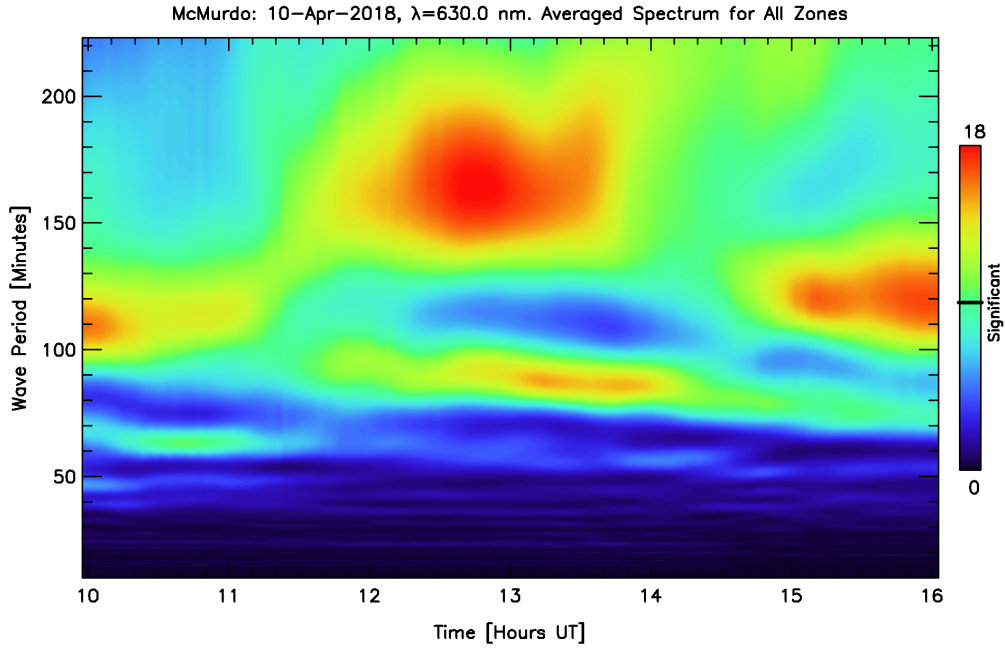


Figure 14. Same as Figure 12 but for F-region wind oscillations.

591 Note that the dynamic spectra showed substantial variability in wave periods from
 592 zone to zone. Wave periods that were statistically significant in a specific viewing zone
 593 were not necessarily significant in the all-sky dynamic spectrum.

594 In principle, these instruments could introduce oscillatory artifacts, for example,
 595 due to oscillations in etalon control parameters such as temperature. However, as dis-
 596 cussed previously, any such instrumental oscillations would almost certainly affect all zones
 597 similarly. The fact that unique oscillations were seen only in a subset of the zones strongly

suggests that these spectra were not instrumental artifacts. On some nights, the Lomb-Scargle analysis of data from some zones showed no periods with statistically significant wave power. Such instances were rare but did occur for some days that are included in this study.

4 Discussion

4.1 Artifacts due to E-region Emission Height Variation

Substantial oscillations in LOS wind at F-region altitudes were detected frequently. By contrast, the SDI data contained fewer instances of clear wavelike oscillations in either F-region temperature or E-region LOS winds. Even though the 558 nm Doppler shift and Doppler width are accurately determined by the instrument with a high signal-to-noise ratio, interpretation of these quantities is complicated by the changing height of the green-line emission layer. In the case of deriving temperatures from Doppler widths, the vertical temperature gradient is so strong in the E-region that the dominant perturbations in high pass filtered 558 nm temperature time series arise simply because of the emission height variations due to changing characteristic energy of the auroral precipitation that excites the emission. Thus, although oscillations were seen in E-region temperatures, we presume that these mostly would have been due to changes in the aurora rather than the actual fluctuations in the background temperature at a constant height. In the case of 558 nm LOS wind measurements, the vertical gradients of horizontal wind in the E-region can also be strong (Larsen, 2002; Branning et al., 2022), which means that height variations of the emission layer may add artifacts to the high pass filtered LOS wind time series that could, at times, dominate over other signals, such as those that might indicate the presence of atmospheric waves. Periods when such artifacts appear can be easily identified as “bursts” of noise in the wind time series correlated with periods when the 558 nm Doppler temperature is changing rapidly. An example of such behavior is shown in Figure 15. In this figure, the fitted zonal wind is noisy and variable when the fitted temperature is more variable. Note that much of the variability indicated by the wind error bars arises not because the fitted winds have large uncertainty but because the fitted wind field is non-uniform. Temperature variations indicate changes in the emission height - and that could mean the measured winds would change if there was a strong vertical gradient in the wind field. In this experiment, there is no way to determine whether strong vertical gradients were present - but the figure at least shows

that some of the wind variability could be associated with height changes. Such changes, if they do occur, would contribute to perturbations in the wave plots. However, an examination of roughly 20 years of 558 nm SDI data shows that the strength of this contribution can be quite variable. Overall, it is thus not surprising that E-region wind oscillations look noisier in the SDI data than those generally observed for F-region winds.

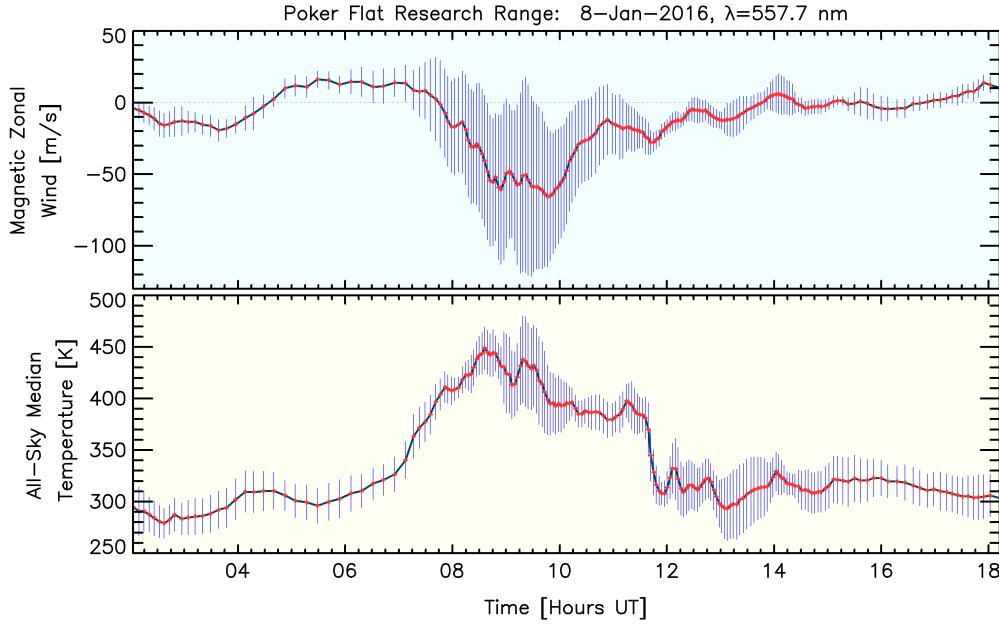


Figure 15. Fitted temperatures and winds derived from 558 nm spectra for Jan 8, 2016, at Poker Flat. The top and bottom panels respectively show the fitted zonal wind speeds and all-sky median temperatures as a function of time. In both panels, the “error bars” show the standard deviation of the corresponding 115 values of the fitted quantity at each observing time. Thus, the error bars are not solely indicating statistical uncertainty in the measurements – in many cases, longer error bars arise because of true geophysical variability across the field of view (however, statistical uncertainty will always have some contribution.)

4.2 Qualitative Testing of the Plausibility of Wave Interpretation

SDI instruments have multiple viewing zones that project to an extended geographic region in the thermosphere. For waves propagating across the instrument’s field of view, systematic delays are expected between the times at which a given phase front would cross viewing zones that are separated with respect to each other along the direction of

640 wave propagation. There should thus be systematic phase differences between pertur-
 641 bations observed by the individual zones, with the particular pattern of phase differences
 642 being characteristic of the speed and direction of the wave's phase propagation. Further,
 643 the observed LOS wind oscillation is typically modulated in part by the viewing azimuth.
 644 This is because the contribution to the observed wave perturbation is modulated by the
 645 dot product of the viewing azimuth direction and the direction of horizontal motion as-
 646 sociated with the wave. Note that no such viewing azimuth dependence applies to the
 647 LOS component of vertical wave oscillations. Rather, this contribution is instead mod-
 648 ulated by the cosine of the observing zenith angle.

649 If wind perturbations occurring in the atmosphere were only in the horizontal com-
 650 ponents, the amplitude of the LOS component of this oscillation would be zero when look-
 651 ing in the zenith and, for other look directions, it would increase in proportion to the
 652 sine of the zenith angle. In most instances, this general behavior was observed for the
 653 LOS wind, although the amplitude of the oscillation in the zenith zone was almost never
 654 seen to drop entirely to zero. Usually, small but non-zero oscillation amplitudes were ob-
 655 served in the zenith zone, with the amplitude of these oscillations increasing with zenith
 656 angles (as expected) out to a maximum near the horizon. These characteristics indicate
 657 that the wind perturbations had both horizontal and vertical components associated with
 658 them, with the horizontal component typically being larger. The observed systematic
 659 dependence of LOS wind perturbation amplitude on the zenith angle would be extremely
 660 unlikely to arise purely because of instrumental artifacts. Instead, observed perturba-
 661 tions are almost certainly of geophysical origin. Temperature oscillations are, by con-
 662 trast, scalar quantities that would not manifest any amplitude dependence on zenith or
 663 azimuth angle – which was largely consistent with the actual behavior observed. Nev-
 664 ertheless, a small level of zenith angle dependence was seen in the temperature oscilla-
 665 tions as well. The exact reason for this weak effect is unknown, although one possibil-
 666 ity involves the changing volume of the atmosphere enclosed by the intersection of the
 667 airglow layer with the solid angle viewed by each zone.

668 Moreover, for a uniform field of monochromatic plane phase fronts, and a given zenith
 669 angle, there would be a pair of diametrically opposite azimuths for which the LOS com-
 670 ponents of the horizontal wind oscillation amplitudes would maximize, and they would
 671 be zero when viewing perpendicular to those azimuths. However, as depicted in Figure
 672 16 (and in most other cases inspected), such simple and systematic azimuthal variation

of perturbation amplitudes were not observed. It is inferred from this that the actual
wind perturbations in the SDI data were usually not due to a uniform field of monochro-
matic waves in the horizontal wind. Rather, the actual wave fields in the thermosphere
must always be more complicated indicating, for any given time, the presence of a range
of periods and multiple propagation directions within the field of view. Nevertheless, Fig-
ure 16 clearly shows that the wind oscillation phase does vary with azimuth, as expected
for a geophysical field of propagating waves.

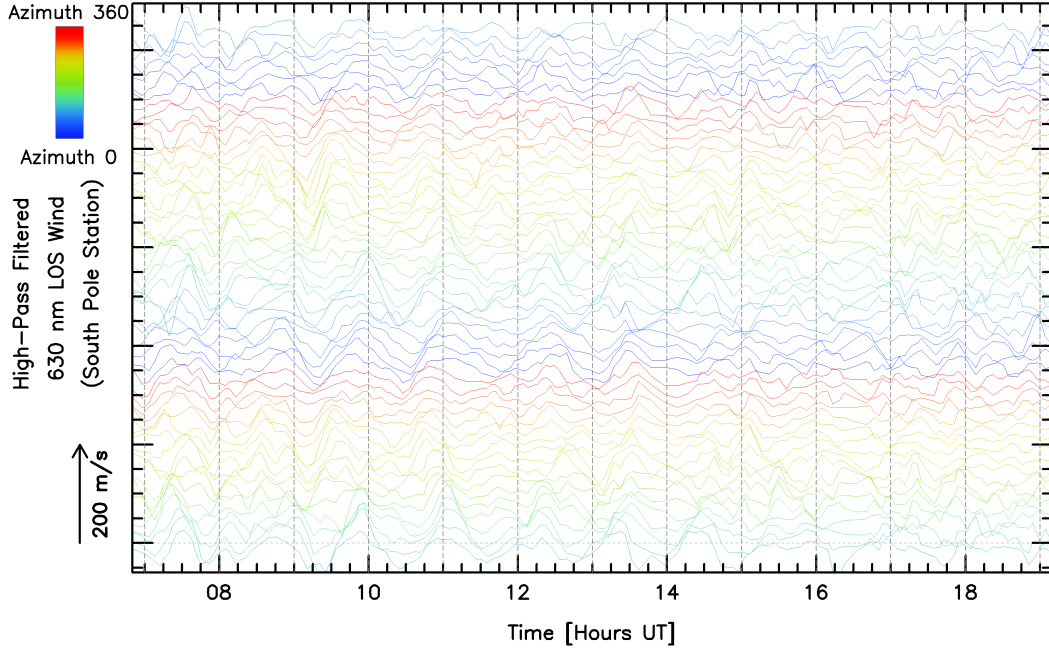


Figure 16. High-pass filtered LOS wind perturbations for selected zones spanning the two outermost rings of the SDI field of view (zones 63 to 114) on April 10, 2018, as observed from the South Pole Station (same day as in the middle panel of Figure 2). The reason for selecting just two rings is to allow phase relationships between successive zones to be more readily discernible.

As expected, instances of relative phase differences between oscillations in differ-
ent zones were frequently seen. However, there were other times when no phase differ-
ences between oscillations were seen regardless of the look azimuths and look elevations.
These events were characterized by large amplitude fluctuations occurring almost time-
synchronously across much of the field of view. Such attributes arise in the SDI data as
shown, for example, in the top two panels of Figure 3 at $\sim 8:30$ UT and in the 558 nm
wind panel of Figure 6 at ~ 11 UT. These time-synchronous responses cannot be signa-

tures of propagating waves. Rather, two possible ways in which such signatures could arise in the SDI data can be postulated.

Firstly, impulsive changes in magnetospheric forcing can impact a wide geographic area of the thermosphere simultaneously. These signatures could thus indicate directly-driven atmospheric perturbations responding simultaneously over a wide geographic area to sudden changes in magnetospheric forcing. The result would be a time-synchronous response across most if not all of the SDI instrument's field of view. It is noted, however, that even if the wind changes time-synchronously, amplitude and phase shifts in the observed LOS wind components are still expected due to the projection angle with varying viewing azimuth. (No such azimuth dependency is expected for temperature perturbations.)

A second (and perhaps more significant) issue arises because sudden changes in auroral precipitation can cause this remote sensing technique to introduce artifacts in the measured winds and temperatures. For example, the time variation of emission brightness can distort recorded spectra because of the way the etalon scans over time, particularly for zones near the zenith. More importantly, as described previously, the altitude of the observed emission can change in response to changing characteristic energy of auroral precipitation. If the observed quantity (wind or temperature) varies with height in the background atmosphere, then the change in characteristic energy will cause changes in the measurements that do not reflect any actual temporal change in the real atmosphere (Sica et al., 1986; McCormac et al., 1987).

Time-synchronous events typically occurred superposed upon a preexisting ambient wave field. Nevertheless, the time-synchronous events almost always were observed during times of substantial impulsive auroral and geomagnetic forcing of the atmosphere. This forcing often excited significant oscillations that were resolvable for several hours after the initial event. Thus, even though the time-synchronous perturbations do not appear to themselves be signatures of wave perturbations, they usually indicated the onset of forcing events that did produce subsequently observable waves.

Time-synchronous perturbations can be identified readily in the SDI data but may not be as conspicuous to an instrument with observations in only a few look directions. Observations based on a single or small number of look directions would be unable to distinguish between traveling waves and time-synchronous non-wavelike oscillations, due

to the inability to track phase shifts among the different look directions. This could lead every oscillation to be interpreted as a signature of a traveling wave. However, as explained above, this current study has shown that there are many instances when such an assumption would be likely to be incorrect, at least for large perturbations observed in auroral latitudes. We, therefore, caution that inferences regarding wave activity that are based on Doppler spectral observations incorporating only a small number of look directions (or possibly only one) might be biased by artifacts associated with the types of time-synchronous responses that have been identified here.

As discussed in earlier sections, waves in the thermosphere do not exclusively originate in situ. Some portion of the wave spectrum is caused by driving that occurs in the lower atmosphere, with perturbations subsequently propagating up to the thermosphere, albeit possibly after one or more instances of breaking and exciting secondary waves (Smith et al., 2013; Vadas et al., 2018). During this process of wave breaking and critical layer filtering, the original shorter-period waves typically fail to reach thermospheric heights. Further, the dissipation of waves as a result of rapid diffusion suppresses short-period waves in the F-region (Fritts & Alexander, 2003). Based on these considerations, the resulting F-region wind oscillations would be expected to be smoother (with less power at high frequencies) than the corresponding E-region oscillations. The observations were indeed consistent with this expectation.

4.3 Quantitative Consistency Tests

As noted, it is difficult to know the extent to which the oscillations observed here are due to atmospheric gravity waves, versus other geophysical processes or (possibly) instrumental mechanisms. However, one potential “back-of-the-envelope” diagnostic is to test whether relations between observed perturbations in the horizontal wind, vertical wind, and temperature are at least not inconsistent with theoretical expectations for thermospheric gravity waves. Application of simplified gravity wave polarization relations for a harmonic oscillation (e.g., Hines, 1960) predicts the following relationships between the various wave perturbation amplitudes and wave parameters

$$\frac{u'}{\omega k_x k_z C^2} = \frac{z'}{-\omega k_x^2 C^2} = \frac{\rho'/\bar{\rho}}{i(\gamma - 1) g k_x^2}, \quad (1)$$

where u' and z' are the amplitudes of the wave's horizontal and vertical oscillations respectively, $\rho'/\bar{\rho}$ is the fractional mass density perturbation amplitude, ω is the intrinsic (angular) frequency of the wave oscillation, k_x and k_z are the horizontal and vertical wave numbers, g is the acceleration due to Earth's gravity, γ is the adiabatic constant (with a value of 5/3 for a monatomic gas), and $C = \sqrt{\gamma g H}$ is the speed of phase propagation for sound waves with H being the scale height. Also, i is $\sqrt{-1}$, which merely indicates that the density oscillations are 90° out of phase with the wind oscillations.

Assuming the relative temperature perturbation amplitude T'/\bar{T} is the same as the relative density amplitude, and writing the Brunt-Väisälä frequency as

$$\omega_b \simeq \sqrt{\frac{\gamma - 1}{\gamma} \frac{g}{H}}, \quad (2)$$

Equations (1) can be rearranged to give

$$\frac{T'}{\bar{T}} \simeq \frac{\omega_b^2}{g\omega} z', \quad (3)$$

$$\text{and } \frac{k_x}{k_z} = \frac{z'}{u'}, \quad (4)$$

The quantities u' , z' , T' , \bar{T} , and ω obviously vary considerably among the data examples presented here. For each of these parameters, the largest observed perturbation amplitudes in this study were a factor of ~ 5 times as large as the smallest observed perturbation amplitude. Nevertheless, by examining many days of data, we find that it is possible to meaningfully estimate a “typical” observed amplitude, at least to the precision needed to test whether the results are consistent with gravity wave theory. Resulting estimates for these quantities in the 630 nm (F-region) data were $u' \simeq 50 \text{ m s}^{-1}$, $z' \simeq 20 \text{ m s}^{-1}$, $T'/\bar{T} \simeq 6\%$ (*i.e.*, 50 K/800 K), and $\omega \simeq 2\pi/(3600 \text{ s})$. (Here, z' was estimated from the LOS wind oscillation amplitude in the zenith zone, whereas u' was determined from the amplitudes in the outer zones.)

Inserting the observed estimates for u' and z' into Equation 4 shows that $k_z \simeq 2.5k_x$ for the waves observed here. This can then be substituted into the usual non-dissipative dispersion relation for thermospheric gravity waves (e.g., Vadas & Fritts, 2005)

$$\omega = \sqrt{\frac{k_x^2 \omega_b^2}{k_z^2 + k_x^2 + \left(\frac{1}{2H}\right)^2}} \quad (5)$$

and solved for k_x , from which the horizontal wavelength of these waves (with temporal period $\simeq 60$ minutes) can be estimated to be

$$\lambda_x \simeq 2\pi\sqrt{29}H \simeq 1520 \text{ km}, \quad (6)$$

which was obtained using estimates of $\omega_b \simeq 2\pi/(12 \text{ minutes})$ and $H \simeq 45 \text{ km}$ – which are representative for conditions at F-region heights. The characteristic horizontal intrinsic phase speeds for the observed waves can then be estimated as

$$v_{px} = \frac{\omega}{k_x} = \frac{2\pi/3600 \text{ s}}{2\pi/1520 \text{ km}} \simeq 420 \text{ m s}^{-1}. \quad (7)$$

These horizontal wavelengths and horizontal phase speeds are well within the ranges previously observed for these parameters of thermospheric gravity waves at F-region heights (e.g. Miyoshi et al., 2018; England et al., 2020).

Also, for a Brunt-Väisälä period of 12 minutes, and using the representative values encountered in this study of $\omega \sim 2\pi/(60 \text{ minutes})$ and $z' \sim 20 \text{ m/s}$, the right-hand side of Equation 3 predicts that the relative temperature perturbations due to the observed waves would be around 9%. As calculated previously, the observed relative temperature perturbation is $\sim 6\%$. Here, the predicted T' is a little larger than the observed T' . Although these values are slightly different, several of the contributing factors for T' have large relative uncertainties – i.e., 100% or more. Given the uncertainty in the input values, the calculated T'/\bar{T} is not inconsistent with observations.

Finally, the predicted 90° phase shift between wind and temperature oscillations should provide a demanding test of whether the data are consistent with waves. Unfortunately, the observed waveforms were seldom monochromatic enough for this to be a definitive test. In Figure 17, a small portion of the data was zoomed-in so that the phase relationship can be examined readily by making individual traces apparent. As shown by Figure 17, there was seldom, if ever, a simple phase relation between observed wind and temperature oscillations. In particular, wind oscillations with a period of ~ 60 minutes are easily discernible toward the top of the upper panel of Figure 17. However, the corresponding temperature oscillations are more difficult to discern.

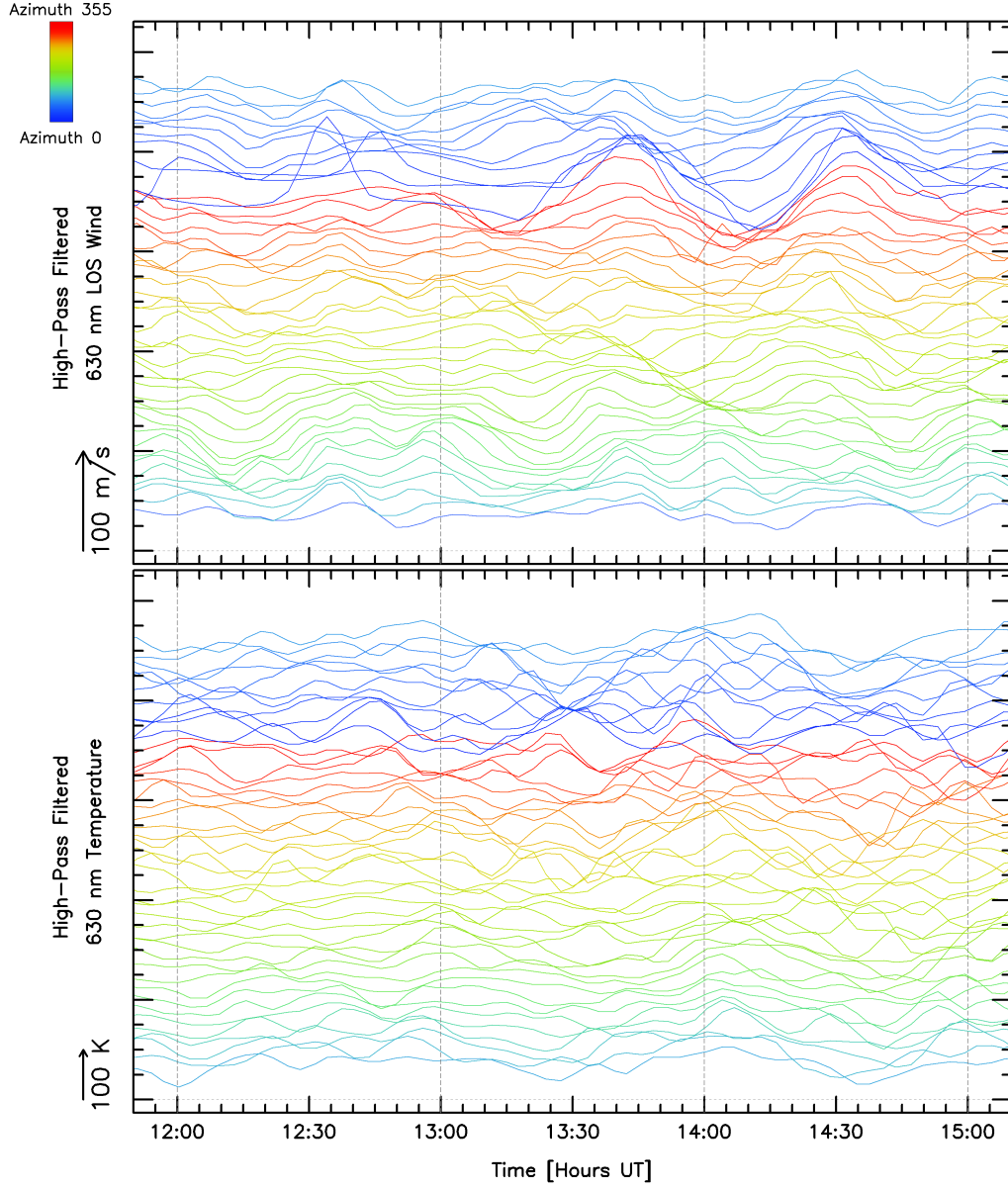


Figure 17. Zoomed-in subset of temperature and LOS wind oscillations observed on Nov 7, 2017, from Poker Flat, Alaska. This figure only shows three hours of data for selected zones (zones 218-261) in the outermost ring of the SDI field of view. These oscillations were generally complicated, such that it is difficult to discern any systematic phase relationship between wind and temperature oscillations.

795 It seems likely that the perturbations observed here are signatures of important pro-
 796 cesses in the thermospheric energy and momentum budgets. It is, therefore, crucial to

understand the extent to which these perturbations are representative of traveling waves propagating in the real thermosphere. The next step would be to use the SDI data to investigate the distributions of phase speeds, horizontal wavelength, vertical wavelength, propagation directions, intrinsic periods, etc. Robust reconstruction of phase fronts would be facilitated by the multiple observing stations and look directions provided by the SDI instrument array. It would then be possible to infer the various wave parameters. However, this analysis would require fitting a two-dimensional field of traveling phase fronts to the data, which itself is a non-trivial forward modeling problem even if there is just one simple monochromatic plane wave field present. If there are multiple wave packets, each with their own individual amplitudes, phase, propagation direction, period, etc., the analysis would become far more difficult.

As a final note, this study required manual inspection of hundreds of days of data from each site. Statistical metrics have not yet been developed to rigorously quantify the occurrence frequency of discernible wave activity. However, qualitatively, it was noticed that truly quiescent conditions were uncommon in the F-region above most of the SDI sites. For all but one site, it was unusual to encounter a day when the instrument was functioning well, and the sky was clear, but the F-region wave signal was indistinguishable from noise. The one exception to this was the site at Mawson, for which the impression was formed that quiescent days were more common. To test this, approximately 130 clear nights of high-pass filtered 630 nm LOS wind data were examined. These observations were acquired from Mawson in 2011. We were unable to confidently recognize wave perturbations on roughly 40% of these days. By contrast, the unambiguous absence of waves was rare for all other sites. These results suggest that the wave field above Mawson can relax to a more quiescent state than it can elsewhere. One possible interpretation is that there is a background contribution of waves propagating up from the lower atmosphere that is seen by most sites apart from Mawson. This perhaps indicates that the orographic and/or meteorological generation of lower atmospheric waves is less significant at this site.

5 Conclusions

This study examined oscillatory perturbations in measurements of thermospheric temperature and wind derived from optical Doppler spectra. Significant oscillatory perturbations were unambiguously detected using high-pass temporal filtering. Their char-

acteristics suggest that they are of geophysical origin. The objective of studying them was to examine the hypothesis that these perturbations could be signatures of gravity wave activity. Perturbation amplitudes were observed to increase considerably during increased geophysical activity. While F-region wind perturbations were almost always detected at some level, the SDI instruments were less able to resolve oscillations in F-region temperatures or E-region winds. This is understood as arising because the perturbation amplitudes of F-region temperature and E-region winds are smaller relative to other sources of measurement variability and errors for these quantities. Nevertheless, the data do contain instances of apparent wavelike perturbations in those quantities as well.

The dependence of the perturbation amplitudes on geophysical activity, viewing zenith angle, and viewing azimuth angle all indicate that the observed fluctuations were of geophysical origin rather than being due to measurement artifacts. Phase relations between the time series for the various viewing zones suggest that the observed perturbations were often consistent with expectations for a (typically complicated) field of traveling waves, although this was not always the case. Many instances of time-synchronous perturbations across all viewing zones were observed, that cannot be interpreted as signatures of waves.

Nevertheless, the data suggest that the technique can detect thermospheric gravity waves and, further, it shows that wave activity is common in Earth's thermosphere at auroral latitudes. Additionally, the data suggest that the wave response to the geomagnetic activity is similar in either hemisphere.

Azimuthal variation of phases throughout all of the data suggests that the wave field in the Earth's thermosphere is seldom a simple set of monochromatic plane phase fronts. Rather, it appears that the wave field is more typically composed of many different wave packets with widely varying amplitudes, phases, and propagation directions. Presumably, if such wave fields could be visualized, they would appear reminiscent of the complicated field of surface waves often seen on the ocean.

Sliding-window Lomb-Scargle analysis was performed on the LOS wind time series from selected nights to analyze how the spectrum of observed wave periods varied as a function of time during the night. The resulting periodograms showed that the wave spectra varied from zone to zone. Further, spectra also varied within individual zones

over the course of a night. The shortest observed periods for F-region wind oscillations with statistically significant power were typically 60 minutes. By contrast, the spectrum of E-region waves extended to shorter periods – i.e., as short as 30 minutes. Oscillations with periods up to 220 minutes were detected both at E- and F-region altitudes. Longer-period oscillations may occur, but those cannot be resolved with the current technique. Thermospheric gravity waves have been observed in previous studies over a broad range of periods extending from a few tens of minutes up to more than 12 hours (Richmond, 1978; Vadas & Fritts, 2006; Ford et al., 2008; Klausner et al., 2009; Katamzi-Joseph et al., 2019). The wave periods observed here fall well within this range. Observed E-region wind oscillations were often noisier and less monochromatic than the corresponding F-region wind perturbations, resulting in broader Lomb-Scargle spectra for E-region data. As discussed in section 3.1.4, geophysical noise due to the altitude variation of the 558 nm emission layer could have contributed to this spectral broadening of the E-region time series. By contrast, the F-region LOS wind oscillations were relatively smooth, as expected.

The initial expectation was that oscillations observed during quiet geomagnetic conditions could be indications of disturbances propagating up from below, because in-situ wave generation would, presumably, be weak. Although wave perturbations likely do propagate up from the lower atmosphere, this study did not resolve such a component, because of the nearly ubiquitous background activity. More detailed analysis will be required to determine the relative contributions of in-situ forcing versus upward propagation.

There is more information in the SDI data than has been examined in this current work. Future studies will focus on phase lags and relative amplitudes of oscillations between time series recorded in different zones. Although relatively rare, it is expected that there would be some instances when the wave field is sufficiently simple that the relative amplitudes and phases between the zones could be used to infer the properties of at least the dominant perturbations that are present. Measuring these phase lags would characterize properties such as the period, phase speed, and direction of phase propagation. This analysis would not be possible for observations made in a single look direction and would be less robust if only a small number of directions were viewed.

Acknowledgments

This research was supported by NSF award numbers 1341545 and 1452333. Magnetometer observations used in this work were provided by Geosciences Australia (Mawson), the New Zealand Antarctic Program (Scott Base), and the US Geological Survey (College), and accessed via the archive maintained by the International INTERMAGNET program (www.intermagnet.org). We also thank INTERMAGNET for promoting high standards of magnetic observatory practice. Scanning Doppler Imager data are available at http://sdi_server.gi.alaska.edu/sdi_web_plots. Solar radio flux density (F10.7) data were adopted from <https://www.spaceweather.gc.ca/forecast-prevision/solar-solaire/solarflux/sx-5-flux-en.php>.

References

- Anderson, C., Conde, M., & McHarg, M. (2012a). Neutral thermospheric dynamics observed with two scanning doppler imagers: 1. monostatic and bistatic winds. *Journal of Geophysical Research: Space Physics*, 117(A3).
- Anderson, C., Conde, M., & McHarg, M. (2012b). Neutral thermospheric dynamics observed with two scanning doppler imagers: 3. horizontal wind gradients. *Journal of Geophysical Research: Space Physics*, 117(A5).
- Branning, K., Conde, M., Larsen, M., & Troyer, R. (2022). Resolving vertical variations of horizontal neutral winds in earth's high latitude space-atmosphere interaction region (sair). *Journal of Geophysical Research: Space Physics*, 127(5), e2021JA029805.
- Bruinsma, S. L., & Forbes, J. M. (2008). Medium-to large-scale density variability as observed by champ. *Space Weather*, 6(8).
- Conde, M., Bristow, W., Hampton, D., & Elliott, J. (2018). Multiinstrument studies of thermospheric weather above alaska. *Journal of Geophysical Research: Space Physics*, 123(11), 9836–9861.
- Conde, M., Craven, J., Immel, T., Hoch, E., Stenbaek-Nielsen, H., Hallinan, T., ... others (2001). Assimilated observations of thermospheric winds, the aurora, and ionospheric currents over alaska. *Journal of Geophysical Research: Space Physics*, 106(A6), 10493–10508.
- Conde, M., & Smith, R. (1998). Spatial structure in the thermospheric horizontal wind above poker flat, alaska, during solar minimum. *Journal of Geophysical Research*

- 924 *search: Space Physics*, 103(A5), 9449–9471.
- 925 Djuth, F., Sulzer, M., Elder, J., & Wickwar, V. (1997). High-resolution studies
926 of atmosphere-ionosphere coupling at arecibo observatory, puerto rico. *Radio Sci-*
927 *ence*, 32(6), 2321–2344.
- 928 Djuth, F., Sulzer, M., Gonzales, S., Mathews, J., Elder, J., & Walterscheid, R.
929 (2004). A continuum of gravity waves in the arecibo thermosphere? *Geophysical*
930 *Research Letters*, 31(16).
- 931 England, S. L., Greer, K. R., Solomon, S. C., Eastes, R. W., McClintock, W. E., &
932 Burns, A. G. (2020). Observation of thermospheric gravity waves in the southern
933 hemisphere with gold. *Journal of Geophysical Research: Space Physics*, 125(4),
934 e2019JA027405.
- 935 Ford, E., Aruliah, A., Griffin, E., & McWhirter, I. (2008). Statistical analysis of
936 thermospheric gravity waves from fabry-perot interferometer measurements of
937 atomic oxygen. In *Annales geophysicae* (Vol. 26, pp. 29–45).
- 938 Fritts, D. C., & Alexander, M. J. (2003). Gravity wave dynamics and effects in the
939 middle atmosphere. *Reviews of geophysics*, 41(1).
- 940 Fukushima, D., Shiokawa, K., Otsuka, Y., & Ogawa, T. (2012). Observation of
941 equatorial nighttime medium-scale traveling ionospheric disturbances in 630-nm
942 airglow images over 7 years. *Journal of Geophysical Research: Space Physics*,
943 117(A10).
- 944 Gabrielse, C., Nishimura, T., Chen, M., Hecht, J. H., Kaeppler, S. R., Gillies, D. M.,
945 ... Evans, J. S. (2021). Estimating precipitating energy flux, average energy, and
946 hall auroral conductance from themis all-sky-imagers with focus on mesoscales.
947 *Frontiers in Physics*, 9, 744298.
- 948 Galvan, D. A., Komjathy, A., Hickey, M. P., & Mannucci, A. J. (2011). The 2009
949 samoa and 2010 chile tsunamis as observed in the ionosphere using gps total elec-
950 tron content. *Journal of Geophysical Research: Space Physics*, 116(A6).
- 951 Garcia, R. F., Bruinsma, S., Massarweh, L., & Doornbos, E. (2016). Medium-scale
952 gravity wave activity in the thermosphere inferred from goce data. *Journal of*
953 *Geophysical Research: Space Physics*, 121(8), 8089–8102.
- 954 Hays, P., Nagy, A. F., & Roble, R. (1969). Interferometric measurements of the 6300
955 a doppler temperature during a magnetic storm. *Journal of Geophysical Research*,
956 74(16), 4162–4168.

- 957 Hecht, J., Strickland, D., & Conde, M. (2006). The application of ground-based
958 optical techniques for inferring electron energy deposition and composition change
959 during auroral precipitation events. *Journal of atmospheric and solar-terrestrial*
960 *physics*, 68(13), 1502–1519.
- 961 Hernandez, G. (1982). Vertical motions of the neutral thermosphere at midlatitude.
962 *Geophysical Research Letters*, 9(5), 555–557.
- 963 Hickey, M., Schubert, G., & Walterscheid, R. (2010). Atmospheric airglow fluctu-
964 ations due to a tsunami-driven gravity wave disturbance. *Journal of Geophysical*
965 *Research: Space Physics*, 115(A6).
- 966 Hines, C. O. (1960). Internal atmospheric gravity waves at ionospheric heights.
967 *Canadian Journal of Physics*, 38(11), 1441–1481.
- 968 Hocke, K., Schlegel, K., et al. (1996). A review of atmospheric gravity waves and
969 travelling ionospheric disturbances: 1982–1995. In *Annales geophysicae* (Vol. 14,
970 p. 917).
- 971 Innis, J. (2000). Deceleration of the high-latitude thermospheric wind by polar cap
972 gravity waves. *Geophysical research letters*, 27(23), 3813–3816.
- 973 Innis, J., Greet, P., & Dyson, P. (1996). Fabry-perot spectrometer observations of
974 the auroral oval/polar cap boundary above mawson, antarctica. *Journal of Atmo-*
975 *spheric and Terrestrial Physics*, 58(16), 1973–1988.
- 976 Itani, R., & Conde, M. (2021). Characterizing unexpectedly localized slowing of the
977 thermospheric cross-polar jet of neutral wind over alaska in the midnight sector.
978 *Journal of Geophysical Research: Space Physics*, 126(10), e2020JA028916.
- 979 Johnson, F., Hanson, W., Hodges, R., Coley, W., Carignan, G., & Spencer, N.
980 (1995). Gravity waves near 300 km over the polar caps. *Journal of Geophysi-*
981 *cal Research: Space Physics*, 100(A12), 23993–24002.
- 982 Kaeppler, S., Hampton, D., Nicolls, M., Strømme, A., Solomon, S., Hecht, J., &
983 Conde, M. (2015). An investigation comparing ground-based techniques that
984 quantify auroral electron flux and conductance. *Journal of Geophysical Research:*
985 *Space Physics*, 120(10), 9038–9056.
- 986 Katamzi-Joseph, Z. T., Aruliah, A. L., Oksavik, K., Habarulema, J. B., Kauristie,
987 K., & Kosch, M. J. (2019). Multi-instrument observations of large-scale atmo-
988 spheric gravity waves/traveling ionospheric disturbances associated with enhanced
989 auroral activity over svalbard. *Advances in Space Research*, 63(1), 270–281.

- 990 Killeen, T., Craven, J., Frank, L., Ponthieu, J.-J., Spencer, N., Heelis, R., ... Carig-
 991 nan, G. (1988). On the relationship between dynamics of the polar thermosphere
 992 and morphology of the aurora: Global-scale observations from dynamics explorers
 993 1 and 2. *Journal of Geophysical Research: Space Physics*, 93(A4), 2675–2692.
- 994 Killeen, T., & Roble, R. (1988). Thermosphere dynamics: Contributions from the
 995 first 5 years of the dynamics explorer program. *Reviews of Geophysics*, 26(2),
 996 329–367.
- 997 Klausner, V., Fagundes, P., Sahai, Y., Wrasse, C., Pillat, V., & Becker-Guedes, F.
 998 (2009). Observations of gw/tid oscillations in the f2 layer at low latitude during
 999 high and low solar activity, geomagnetic quiet and disturbed periods. *Journal of*
 1000 *Geophysical Research: Space Physics*, 114(A2).
- 1001 Larsen, M. (2002). Winds and shears in the mesosphere and lower thermosphere:
 1002 Results from four decades of chemical release wind measurements. *Journal of Geo-*
 1003 *physical Research: Space Physics*, 107(A8), SIA–28.
- 1004 Lomb, N. R. (1976). Least-squares frequency analysis of unequally spaced data. *As-*
 1005 *trophysics and space science*, 39(2), 447–462.
- 1006 McCormac, F., Killeen, T. L., Nardi, B., & Smith, R. (1987). How close are
 1007 ground-based fabry-perot thermospheric wind and temperature measurements
 1008 to exospheric values? a simulation study. *Planetary and space science*, 35(10),
 1009 1255–1265.
- 1010 Miyoshi, Y., Jin, H., Fujiwara, H., & Shinagawa, H. (2018). Numerical study of
 1011 traveling ionospheric disturbances generated by an upward propagating gravity
 1012 wave. *Journal of Geophysical Research: Space Physics*, 123(3), 2141–2155.
- 1013 Nicolls, M., Vadas, S., Meriwether, J., Conde, M., & Hampton, D. (2012). The
 1014 phases and amplitudes of gravity waves propagating and dissipating in the ther-
 1015 mosphere: Application to measurements over alaska. *Journal of Geophysical*
 1016 *Research: Space Physics*, 117(A5).
- 1017 Oliver, W., Otsuka, Y., Sato, M., Takami, T., & Fukao, S. (1997). A climatology of
 1018 f region gravity wave propagation over the middle and upper atmosphere radar.
 1019 *Journal of Geophysical Research: Space Physics*, 102(A7), 14499–14512.
- 1020 Oyama, S., Ishii, M., Murayama, Y., Shinagawa, H., Buchert, S., Fujii, R., & Kof-
 1021 man, W. (2001). Generation of atmospheric gravity waves associated with auroral
 1022 activity in the polar f region. *Journal of Geophysical Research: Space Physics*,

- 1023 106(A9), 18543–18554.
- 1024 Paulino, I., Medeiros, A., Vadas, S., Wrasse, C., Takahashi, H., Buriti, R., . . . others
1025 (2016). Periodic waves in the lower thermosphere observed by oi630 nm airglow
1026 images. In *Annales geophysicae* (Vol. 34, pp. 293–301).
- 1027 Richmond, A. (1978). Gravity wave generation, propagation, and dissipation in
1028 the thermosphere. *Journal of Geophysical Research: Space Physics*, 83(A9), 4131–
1029 4145.
- 1030 Scargle, J. D. (1982). Studies in astronomical time series analysis. ii-statistical
1031 aspects of spectral analysis of unevenly spaced data. *The Astrophysical Journal*,
1032 263, 835–853.
- 1033 Sica, R., Rees, M., Roble, R. G., Hernandez, G., & Romick, G. (1986). The alti-
1034 tude region sampled by ground-based doppler temperature measurements of the oi
1035 15867 k emission line in aurorae. *Planetary and space science*, 34(5), 483–488.
- 1036 Smith, S., Vadas, S., Baggaley, W., Hernandez, G., & Baumgardner, J. (2013).
1037 Gravity wave coupling between the mesosphere and thermosphere over new
1038 zealand. *Journal of Geophysical Research: Space Physics*, 118(5), 2694–2707.
- 1039 Vadas, S. L., & Azeem, I. (2020). Concentric secondary gravity waves in the ther-
1040 mosphere and ionosphere over the continental united states on 25-26 march
1041 2015 from deep convection. *Journal of Geophysical Research: Space Physics*,
1042 e2020JA028275.
- 1043 Vadas, S. L., & Fritts, D. C. (2005). Thermospheric responses to gravity waves: In-
1044 fluences of increasing viscosity and thermal diffusivity. *Journal of Geophysical Re-*
1045 *search: Atmospheres*, 110(D15).
- 1046 Vadas, S. L., & Fritts, D. C. (2006). Influence of solar variability on gravity wave
1047 structure and dissipation in the thermosphere from tropospheric convection. *Jour-*
1048 *nal of Geophysical Research: Space Physics*, 111(A10).
- 1049 Vadas, S. L., & Liu, H.-l. (2009). Generation of large-scale gravity waves and neutral
1050 winds in the thermosphere from the dissipation of convectively generated gravity
1051 waves. *Journal of Geophysical Research: Space Physics*, 114(A10).
- 1052 Vadas, S. L., Zhao, J., Chu, X., & Becker, E. (2018). The excitation of secondary
1053 gravity waves from local body forces: Theory and observation. *Journal of Geo-*
1054 *physical Research: Atmospheres*, 123(17), 9296–9325.
- 1055 Yeh, K. C., & Liu, C. H. (1974). Acoustic-gravity waves in the upper atmosphere.

- 1056 *Reviews of Geophysics*, 12(2), 193–216.
- 1057 Yiğit, E., & Medvedev, A. S. (2012). Gravity waves in the thermosphere during a
1058 sudden stratospheric warming. *Geophysical Research Letters*, 39(21).
- 1059 Yiğit, E., & Medvedev, A. S. (2019). Obscure waves in planetary atmospheres:
1060 on earth and on other planets, internal gravity waves shape the dynamics and
1061 thermodynamics of the atmosphere. *Physics today*, 72(6).
- 1062 Yu, Y. (2007). *Model studies of time-dependent ducting for high-frequency grav-*
1063 *ity waves and associated airglow responses in the upper atmosphere.* University of
1064 Central Florida.